https://doi.org/10.5194/egusphere-2025-3790
Preprint. Discussion started: 15 August 2025

Introducing aerosol-cloud interactions in the ECMWF model reveals new constraints on aerosol representation

Paolo Andreozzi[1, 2, 3, 4], Mark D. Fielding[1], Robin J. Hogan[1], Richard M. Forbes[1], Samuel Rémy[5], Birger Bohn[3], and Ulrich Löhnert[4]

[1]European Centre for Medium-Range Weather Forecasts - Bonn (Germany), Reading (United Kingdom)
[2]Deutscher Wetterdienst - Offenbach (Germany)
[3]Forschungszentrum Jülich - Jülich (Germany)
[4]University of Cologne - Cologne (Germany)
[5]HYGEOS - Lille (France)

Correspondence: Paolo Andreozzi (paolo.andreozzi@ecmwf.int)

Abstract. Realistic number concentrations of aerosol cloud condensation nuclei (CCN) are critical to simulate the Earth's atmosphere radiative budget. However, CCN concentrations are very uncertain, which critically limits our capacity to precisely predict climate change. This is partly because aerosol optical depth (AOD) observations, traditionally used for validation of and assimilation into aerosol models, weakly constrain number concentrations. We introduce aerosol-cloud interactions (ACI) in the European Centre for Medium-Range Weather Forecasts (ECMWF) Integrated Forecasting System (IFS) to simulate the activation of aerosols into cloud droplets driven by aerosol concentrations from the Copernicus Atmosphere Monitoring System (CAMS), using offline computations from a parcel model. Then, we use an 18-year-long series of MODIS cloud droplet number concentrations (N_d) retrievals to tune aerosol size distributions and simulated number concentrations. Finally, we validate the system using AOD observations, all-sky broadband SW fluxes, Angstrom exponent and size spectra from satellite and AERONET. We found that CAMS aerosols allows simulating overall realistic N_d values, but these are systematically overestimated over most of sub-Saharan Africa and underestimated at latitudes higher than 60°N and 45°S. While the first bias hints at issues with carbonaceous aerosols from African wildfires, the high-latitude bias originates from too efficient aerosol scavenging in mixed-phase clouds. We finally show that addressing this last issue dramatically improves simulated clouds over the Southern Ocean. This study showcases that representing ACI in a weather model is a powerful diagnostic tool to improve aerosol representations and processes, potentially informing also applications in climate models.

1 Introduction

The number concentration of cloud condensation nuclei (CCN) is essential for the simulation of realistic liquid- and mixed-phase clouds radiative properties in weather and climate models. The pathway by which the abundance of available aerosol CCNs determines the number concentration of droplets (N_d), and in turn, the cloud droplet effective radius (r_e) is generally referred to as the albedo (or Twomey) effect (Twomey, 1977, 1991). This is the first and best understood of a cascade of aerosol indirect effects (Bellouin et al., 2020; Gordon et al., 2023) on the particle size distribution (PSD) of cloud droplets, with

https://doi.org/10.5194/egusphere-2025-3790
Preprint. Discussion started: 15 August 2025

repercussions on the cloud life cycle, macrophysics and precipitation (Albrecht, 1989; Pincus and Baker, 1994). Such indirect effects are included under the umbrella-term of aerosol-cloud interactions (ACI). Due to the macroscopic role of clouds in the regulation of the Earth's energy budget, quite complex aerosol-cloud interactions (ACI) have been for are considered necessary in global climate models (Menon et al., 2002; Stier et al., 2005; Penner et al., 2006; Bellouin et al., 2011; Mulcahy et al., 2018). However, such representations are still fraught with uncertainties, severely limiting the ability of models to precisely predict climate change due to anthropogenic emissions (Szopa et al., 2023).

Activation of CCN into droplets is described by the Köhler theory (e.g. Pruppacher and Klett, 2010) for heterogeneous nucleation of cloud droplets. The efficiency of CCN in supporting droplet nucleation is notably controlled both by their solubility in water, and the amount of surface available for binding with water molecules. A popular way of describing CCN activation is in the form of the κ-Köhler theory (Petters and Kreidenweis, 2007), where aerosol chemical properties are condensed into a single hygroscopicity parameter κ (Quaas and Gryspeerdt, 2022). Rothenberg and Wang (2016) used this framework in the implementation of an adiabatic parcel lifting model to accurately simulate the maximum supersaturation reached during the ascent of an air parcel. This allows the model to also capture the effect of large sea salt particles to prevent activation of available sulfate (SO_4^{2-}) aerosols (Fossum et al., 2020). It is, however, unclear what relevance this effect has in actual atmospheric conditions, e.g. in terms of regulation of global energy budgets or on the aerosol speciation itself, which could be clarified by more accurate representation of aerosol-cloud interactions in global models.

In the realm of numerical weather prediction (NWP), models typically represent aerosol concentrations diagnostically using climatologies (e.g. Tegen et al., 1997; Bozzo et al., 2020). Such simplified descriptions allow beneficial average aerosol-radiation interaction to be caught while avoiding to resort to computationally costly simulations using prognostic aerosol and chemical tracers, i.e. where they are advected and let interacting fully with other components of the system. Within such simplified descriptions, aerosol-cloud interactions are typically neglected. A previous study by Mulcahy et al. (2014) showed that representing the indirect effect with prognostic aerosol fields has widespread and potentially beneficial impact on the radiative budget of an NWP model. Ahlgrimm et al. (2018) showed that model biases in TOA shortwave (SW) radiative fluxes are dominated by errors in the cloud macrophysics (cloud cover, water phase and content, sub-grid heterogeneity) and also significantly affected by deficiencies in the cloud microphysics, i.e. poor N_d representation and, in turn, r_e values. Global NWP models are also moving toward more complex two-moment cloud schemes (Field et al., 2023), where both water content and droplet number concentrations are prognostic variables; this direction implies an even higher importance of realistic CCN values for the cloud microphysics. Despite this, the uncertainty of the physical processes involved in ACI and the difficulties in providing enough observational constraints (Rasch and Carslaw, 2022) have for long time constituted a major challenge. However, the evolution of such systems towards higher integration of applications, from air quality (Baklanov et al., 2017) to weather forecasts and climate simulations (Palmer et al., 2008) unlocks unprecedented opportunities for the validation of processes and representations. In addition to this, NWP models are thoroughly tested and monitored every day with a wide range of observations, which makes them an important testbed for ACI schemes. This offers the potential to refine these schemes in such a way that can also inform climate models.

https://doi.org/10.5194/egusphere-2025-3790
Preprint. Discussion started: 15 August 2025

The Integrated Forecasting System (IFS) used at the European Centre for Medium-Range Weather Forecasts (ECMWF) is a NWP model used to perform operational global meteorological analysis and forecasts on the medium- (10 days), extended- (42 days) and long- (4 months) range. The IFS also supports a configuration with online chemistry and aerosol tracers developed and maintained within the Copernicus Atmosphere Monitoring Service (CAMS) and denoted as IFS-COMPO (Flemming et al., 2015). In the IFS-COMPO configuration, a bin bulk mass prognostic representation of aerosols is used (Rémy et al., 2022), but their feedback into meteorological fields is only mediated by the direct effect. The IFS currently diagnoses N_d values for the calculation of r_e in liquid clouds using a wind-dependent parametrization that changes between land and sea, but that has no dependence in either climatological or prognostic aerosols. Similarly, the IFS uses fixed N_d values over land and sea for the calculation of cloud-to-rain water auto-conversion rates.

Improving the representation of aerosol-cloud-interactions (ACI) in the IFS is therefore a strategic aim at ECMWF, both for CAMS and NWP forecasts. ACI must also reflect the quality of the information provided by aerosol fields, either in a prognostic or climatological representation, the latter being used for forecasts on the medium-range (up to 10 days) and longer timescales (months). A major goal of this study was to associate as realistic as possible values of droplet number concentrations (N_d) in liquid clouds to aerosol mass mixing ratios (MMR) in the model. In order to achieve this, we designed a method to efficiently constrain simulated number concentrations from prognostic aerosol using an 18-years long dataset of MODIS N_d retrievals. The general concept behind our approach has similarities to that adopted by McCoy et al. (2018), who used near-surface daily-mean aerosols mass concentrations of sulfate and sea salt aerosol from MERRA2 reanalyses to predict MODIS N_d retrievals. In contrast, our method introduces several new aspects: firstly, we simulate the near real-time activation of aerosol particles into cloud droplets using an offline version of the aerosol activation scheme. Secondly, instead of using a fixed level above the surface we systematically collocate aerosols and clouds to accurately assess the atmospheric composition at cloud level. Thirdly, instead of optimizing mass-to-number conversion coefficients, we optimize the underlying particle size distribution (PSD) of the bulk aerosols. By using this approach, we are also in the position to interpret the results of the optimization in terms of aerosol representation and assess consistency with other represented processes, such as the direct radiative effect. Finally, results of the optimization procedure could be tested with simulations using the IFS with prognostic aerosols.

This work has the following structure: Section 2 illustrates the mass-bulk representation of aerosols in the IFS and clarifies the impact of aerosol PSD definitions on particle number concentrations and aerosol optical depth; Section 3 describes the observational data used for this study; Section 4 describes the methodology of the study, including the aerosol activation scheme of the IFS, the datasets of observations and the model data; Section 5 presents and discusses the results of the optimization procedure; Section 6 describes the impact of a modified wet-scavenging scheme for mixed-phase clouds on simulated first indirect effect of aerosols. In Section 7 we provide a summary of findings, together with conclusions and possible future outlooks.

https://doi.org/10.5194/egusphere-2025-3790
Preprint. Discussion started: 15 August 2025

2 Aerosol representations in the IFS

The IFS-COMPO CY49R1.0 is equipped with the IFS-AER single moment aerosol scheme (Rémy et al., 2022), where mass concentrations for each aerosol species are prognostic tracers. Optionally, the model can use a model-derived climatology of aerosols (Bozzo et al., 2020), in which case, the IFS-AER scheme is switched off. Currently, the IFS only includes the direct radiative effect of aerosols. Meteorology impacts aerosol optical properties and, in a prognostic configuration, their production, transport and removal. However, feedbacks of aerosol-related processes on meteorological fields are only mediated by influence of aerosol-radiation interactions on heating rates (semi-direct effect of aerosols).

The IFS represents 8 types of aerosols in a bulk representation. These are listed in Table 1. Among these, sea salt (SS) and mineral dust (DU) aerosol species consist of multiple partitions of a broader particle size range, configuring a so-called mixed binned-bulk aerosol scheme. All aerosols in the IFS interact with radiation by bulk optical properties obtained via Mie computations. To this purpose, they are represented by lognormal number PSD, with median radius r_{med} and shape parameter or geometric standard deviation σ (ECMWF, 2024). The normalized PSD $n(r)$ is given by:

$$n(r) = \frac{N_0}{\sqrt{2\pi}\, r\, \ln\sigma}\, e^{-\frac{\ln^2(r/r_{med})}{2\ln^2\sigma}} \tag{1}$$

where N_0 is the total number density of particles, for multimodal species (sea salt and mineral dust):

$$n(r) = \sum_{i=1}^{N} \alpha_i n_i(r) \tag{2}$$

where i indicates each mode of the distribution and α_i are weight coefficients such that $\sum \alpha_i = 1$. Definitions of aerosol tracers and are reported in Table 1.

Hydrophilic species undergo hygroscopic growth by water uptake - described as a function of relative humidity. This is used to determine refractive index and optical properties used by the radiation scheme. Hydrophilic species are also removed when precipitation occurs, with a fixed mass scavenging rate described in ECMWF (2024) and following Luo et al. (2019).

Aerosols in the IFS are represented as externally-mixed species. This means that optical properties of a mixed population are given by superposition principle from the sum of its components. The model is not able to fully represent those aging processes where organics or black carbon form clusters with sulfate particles in aqueous phase. While such aging processes conserve the mass of the involved species considered as separate entities, they also affect the total number, the PSD and the refractive index of the resulting aged aerosol. To represent aging, the IFS aerosol scheme converts organic matter (OM) from the hydrophobic to the hydrophilic type with an e-folding timescale that can be either prescribed or depending on local chemical composition. In either case, aging does not impact any other chemical or aerosol species, or the refractive index of the aged aerosol. Compared to the hydrophobic type, hydrophilic OM has hygroscopic growth and the refractive index is adjusted to describe the water-aerosol mixture; hydrophilic black carbon (BC) is instead optically identical to the hydrophobic type, which represents pristine soot. In reality, aged BC appears in the form of clusters or chain-like aggregates (e.g. Teng et al. (2019) and references therein) that clump with hydrophilic sulfate (SU), nitrate (NI) and ammonium (AM) salt particles to form highly-soluble, large structures. Observed OM also forms coatings around SU aerosol cores, eventually mixing with soot particles (Yu et al., 2019). While we

https://doi.org/10.5194/egusphere-2025-3790
Preprint. Discussion started: 15 August 2025

Aerosol type	Size bin limits (sphere radius [μm])	ρ [g/cm^3]	r_{med} [μm]	σ
Sea Salt (SS)		1.183	0.1, 1.0	1.9, 2.0
bin 1 (SS1)	0.015-0.25			
bin 2 (SS2)	0.25-2.5			
bin 3 (SS3)	2.5-10			
Mineral Dust (DU)		2.61	0.05, 0.42, 0.79, 16.2	2.2, 1.18, 1.93, 1.53
bin 1 (DU1)	0.03-0.55			
bin 2 (DU2)	0.55-0.9			
bin 3 (DU3)	0.9-20			
Black carbon (BC, BCH)*	0.005-0.5	1.0	0.0118	2.0
Sulfates (SU)	0.005-20	1.76	0.11	1.6
Organic matter (OM, OMH)*	0.005-20	1.3	0.09	1.6
Secondary Organic matter				
Biogenic (SOB)	0.005-20	1.8	0.09	1.6
Anthropogenic (SOA)	0.005-20	1.8	0.09	1.6
Nitrates (NI)	0.03-0.9	1.73	0.0355	2.0
	0.9-20†	1.40	0.199, 1.992	1.9, 2.0
Ammonium (AM)	0.005-20	1.76	0.0355	2.0

Table 1. Characterization of the aerosol species for the IFS CY49R1.0, from Rémy et al. (2022) and ECMWF (2024). All species are hydrophilic, except those marked with †, which are hydrophobic, and those marked with *, which are represented by two tracers, one hydrophilic and one hydrophobic. Hydrophobic tracers are not used for CCN computations. The number ratios of the modes for multimodal PSD are: 0.96 and 0.04 for SS and coarse NI, $0.95, 0.020, 0.028, 3.4\ 10^{-7}$ for DU. Note that, differently than elsewhere, parameters for all species, including sea salt, are reported at 0% relative humidity.

cannot afford to fully address this issue in this study, progressing toward more sophisticated representations of aging processes might be a future area of improvements for CAMS, given the relevance of aging for determining CCN number concentrations and, ultimately, cloud droplet number concentrations.

Aerosol sources depend on the species and can depend on meteorological forcing (SS, DU, SU precursors), chemistry (secondary OM, NI, AM, SU), natural and anthropogenic emissions (SU, AM, NI, OM), including wildfires (OM, BC). In turn, chemical processes also depend on the meteorology and radiative fluxes. Removal of aerosol particles takes place via a range of processes, the most of efficient being wet scavenging by precipitation. Each species has a fixed wet scavenging coefficient indicating the mass fraction to be considered dissolved in cloud water; this value is 0.7 for all hydrophilic species except sea salt, for which it is fixed to 0.9 and ammonium, for which it is 0.8 (ECMWF, 2024). When cloud water is converted to precipitation, the scavenging coefficient determines for each species how much of it shall be removed from the grid-box. In

https://doi.org/10.5194/egusphere-2025-3790
Preprint. Discussion started: 15 August 2025

mixed-phase conditions, a temperature-dependent modulation of the activated fraction from Verheggen et al. (2007) is applied to the precipitating ice-phase fraction of the cloud.

In order to calculate the number concentration of available CCN from aerosol fields, a conversion from mass to number is needed. For a given PSD of (spherical) particles, the ratio of particle numbers per unit mass J is given by:

$$J = \frac{3}{4\pi\rho} \int_{r_{\min}}^{r_{\max}} r^3 n(r)\, \mathrm{d}r \tag{3}$$

where the definite integral has an analytical solution when the domain coincides with the set of real numbers $\mathbb{R}$:

$$J = \frac{3}{4\pi\rho} \frac{1}{r_{\text{med}}^3} e^{-9/2 \ln^2 \sigma} \tag{4}$$

where we explicated the dependency of the number-to-mass ratio on the median radius r_{med}. Thereby, each tracer definition defines a map between the mass and number representation given by Equation 4.

Observations of aerosol optical depth (AOD), particulate matter (PM), surface concentrations of speciated aerosols, as well as deposition fluxes are used to constrain aerosols in the IFS; AOD is also operationally assimilated to produce CAMS analyses (Benedetti et al., 2009). However, these observed quantities offer very little information about aerosol number concentrations. This is also the case for AOD, despite it depending on assumptions made on optics (refractive index), physical shape and PSD. To illustrate this, Figure 1 shows the dependency on r_{med} of J together with the $500\,\mathrm{nm}$ mass extinction coefficient (k_{ext}) for a selection of IFS aerosol tracers at different values of relative humidity, which was calculated using the Mie theory for spherical particles. In most cases, curves are quite flat at the default value of r_{med}, which means that k_{ext} is almost independent of small displacements of the PSD. This property derives from the fact that the population is dominated by particles with radius r such the ratio $x = 2\pi\lambda/r$ in the visible regime is close to the peak $x \approx 6$ of the Mie extinction efficiency (Petty, 2006). Relatively small rigid displacements of the PSD of species providing CCN generally have negligible impact on k_{ext}, but large on J (1-2 orders of magnitude). The same holds also for small changes in the shape parameter σ (not shown). Given that AOD in the visible range (400 to $800\,\mathrm{nm}$) is a weak constraint for aerosol particle numbers in a bulk representation, we aim at making modest changes to the PSD assumptions of aerosols in order to optimize the prediction of N_d, while keeping the setup physically consistent with the AOD currently simulated by the system.

3 Observations and datasets

3.1 MODIS AOD and N_d

The MODerate Resolution Imaging Spectroradiometer (MODIS) is mounted on board the polar-orbiting Aqua and Terra satellites operated by NASA. For this study, we use monthly Collection 6.1 level 3 $550\,\mathrm{nm}$ AOD observations covering the period 2003-2024 (Platnick et al., 2017a, b), produced with the Dark Target retrieval algorithm over land and sea (Levy et al., 2013; Sayer et al., 2014).

https://doi.org/10.5194/egusphere-2025-3790
Preprint. Discussion started: 15 August 2025

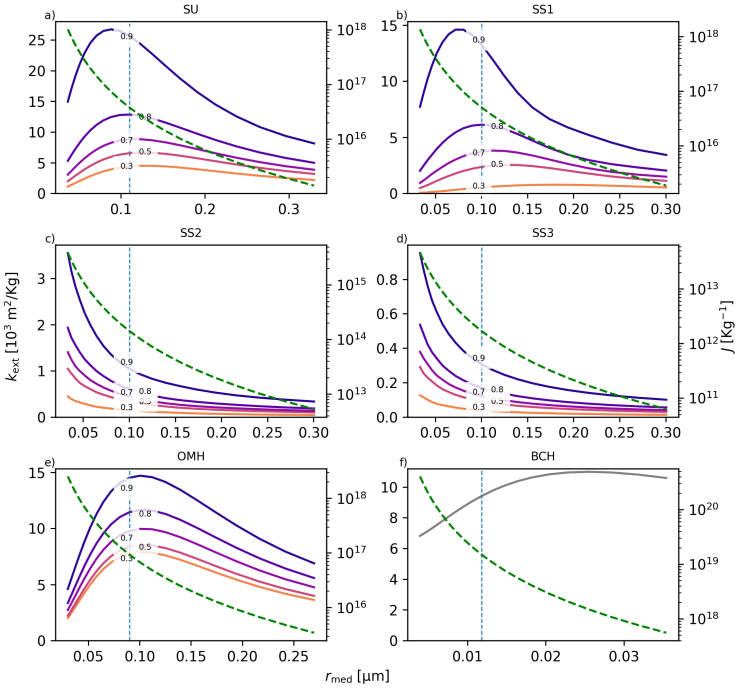

Figure 1. Mass extinction coefficients k_{ext} and number per unit mass J (as defined in Equation 4) as a function of the median radius r_{med} of the number PSD for the hydrophilic aerosol species listed in Table 1. Labels indicate curves corresponding to a selection of relative humidity values. Nitrates and ammonium are not shown, but their optical properties are very close to sulfates for the purpose of this discussion. The dashed green line shows the number of particles per unit mass J as a function of r_{med} and its scale is given on the right of each plot. For each tracer, the vertical dashed line indicates the default dry median radius according to Table 1. For sea salt, the ratio between the two modes median radii $r_{\text{med},2}/r_{\text{med},1}$ was kept constant, and the dashed line indicates the location of the finer mode.

We also use daily MODIS N_d retrievals (Gryspeerdt et al., 2022a) produced by combining Level 2 MODIS retrievals of cloud optical thickness τ and cloud top r_e (Platnick et al., 2017c) under adiabatic (non-precipitating, non-mixing) cloud assumptions. The datasets are describe by Gryspeerdt et al. (2022b) and we used data for the period 2003-2020 on a $1^\circ \times 1^\circ$ rectangular grid. The N_d satellite products computed from bi-spectral retrievals of cloud optical thickness (τ) and effective radius (r_e) (Nakajima and King, 1990) assuming adiabatic profiles for stratocumulus clouds and only including pixels with liquid-phase clouds with cloud-top temperature more than 268 K (see Gryspeerdt et al. (2022b) and references therein). Each N_d dataset is the result of different sampling strategies to target systematic error sources affecting satellite retrievals. The least restrictive sampling strategy is labelled Q06 and selects pixels with retrieved effective radius (r_e) larger than 4 µm, and a minimum cloud optical thickness τ of 4. We also make use of two other sampling strategies from the Gryspeerdt et al. (2022b) paper. One

https://doi.org/10.5194/egusphere-2025-3790
Preprint. Discussion started: 15 August 2025

is named G18, which also requires a pixel cloud fraction larger than 0.9 as well as minimal satellite and solar zenith angles, to address uncertainties associated with cloud measurements under slanted views (e.g. Maddux et al., 2010). The other one is BR17, which, on top of all the above-mentioned filters, also excludes all pixels for which the r_e retrieval does not strictly increase with the wavelength of the deployed near-infrared channel ($1.6\,\mu\mathrm{m}$,$2.2\,\mu\mathrm{m}$ or $3.6\,\mu\mathrm{m}$); this was meant to discard non-adiabatic cloud profiles (see Gryspeerdt et al. (2022b) for a detailed discussion).

For this study, we down-sampled the retrievals (Q06, G18 and BR17) to monthly means and re-gridded them to a $3^\circ \times 3^\circ$ rectangular grid. We use Q06 as the tuning target, while we take the spread across the three datasets to estimate the uncertainty of observations. For each pixel, error bars are defined as the full dispersion (maximum minus minimum) of values across the three datasets. If data are missing in one of the datasets (because there are no valid retrievals satisfying the more restrictive sampling method), the assigned relative error is 1. By doing this we aim at producing error bars that reflect the sensitivity of N_d numbers on every strategy aimed at removing specific sources of error and use this as an indicator of the reliability of the retrieved values.

3.2 VIIRS AOD and AE

The visible Infrared Imaging Radiometer Suite (VIIRS) is mounted on board the Suomi National Polar-orbiting Partnership (SNPP) and NOAA-20 satellites, operated by NOAA. We use the Level 3 monthly $550\,\mathrm{nm}$ AOD and $550\,\mathrm{nm} - 865\,\mathrm{nm}$ Angstrom exponent (AE) products, produced with the Deep Blue (Hsu et al., 2013) retrieval algorithm over land and the Satellite Ocean Aerosol (SOAR) (Sayer et al., 2018) algorithm over sea. for the period 2023-2024(SSEC, 2023a, b).

3.3 AERONET AOD, AE and size spectra

The Aerosol Robotic Network (AERONET) is an extensive network of ground-based sun photometers, providing measurements of aerosol optical properties (Holben et al., 1998). We use daily cloud-cleared, quality-assured and fully-calibrated (Level 2) AOD and AE products, as well as daily cloud-cleared, quality-controlled (Level 1.5) aerosol PSD inversion products (Dubovik and King, 2000) for a selection of observational sites. We used all data between 2003 and 2024 available for each site.

3.4 CERES EBAF TOA broadband shortwave fluxes

The Clouds and the Earth's Radiant Energy System (CERES) instruments for the measurement of top-of-atmosphere (TOA) broadband shortwave (SW) and longwave (LW) radiation (Wielicki et al., 1996) mounted on board the Aqua, Terra, SNPP and NOAA-20 satellites. For this study we use TOA broadband shortwave (SW) all-sky monthly fluxes from Edition 4.2 Energy-balanced and Filled (EBAF) dataset (Doelling, 2022) for the period 2023-2024.

https://doi.org/10.5194/egusphere-2025-3790
Preprint. Discussion started: 15 August 2025

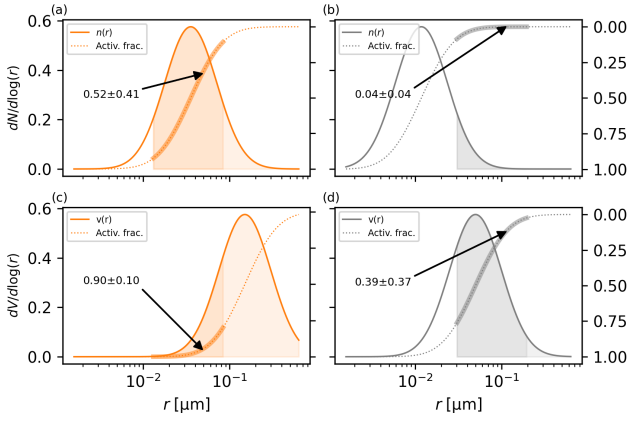

Figure 2. Normalized activated number (a,b) and volume (c,d) fraction for sulfate (a,c) and black carbon (b,d) aerosols in a bulk representation, as a function of critical dry radius. PSD are represented with solid lines, while the activated fractions are reported with dotted lines. The axes on the right show the activated aerosol (mass or number) fraction. Light shadings indicate the activated population, dark shadings show the physical range of variability. Note that the right hand side vertical axis for each plot is directed from top to bottom.

4 Method

We constrained aerosol numbers for the bulk IFS representation with satellite retrievals of droplet number concentrations (N_d). Thereby, we used N_d observations as a tuning target for the N_d values obtained by activation of hygroscopic aerosol species. In order to achieve this, we firstly implemented a lightweight scheme to simulate aerosol activation into droplets that could be used either by the running the IFS (online) or on stored data (offline).

4.1 Activation scheme for the IFS

The activation process of a population of aerosol particles can be summarized in such a way that, depending on local aerosols and thermodynamics (supersaturation), for each species all particles larger than a critical size activate into a droplet. In order to describe the number concentration of droplets we need the number PSD of each CCN species, while to compute the mass eventually scavenged by cloud formation (only with prognostic aerosols) we need their mass PSD. Figure 2 shows particle number and volume (or, equivalently, mass, as we consider one value of density for each species) PSDs and the associated range of dry critical radii under typical atmospheric conditions for boundary layer stratocumuli obtained from parcel simulations (details are provided below). These translate directly into activated mass and number fractions. For sulfates we expect large variability in the number of particles activating into droplets (between 10% and 90%) but small variability in the amount of mass dissolved (between 80% and 100%). For aged black carbon, due to the lower hygroscopicity and smaller typical particle size, we expect the opposite configuration of variability, very small in activated numbers, much larger in activated mass fractions.

https://doi.org/10.5194/egusphere-2025-3790
Preprint. Discussion started: 15 August 2025

Name	κ	r_{med} (µm)	σ	n (cm^{-3})	Recipe
sulfates	0.54	0.11	1.6	$[10, 1000]$	$1m_{\text{SU}}$
nitrates	0.88	0.035	2.0	$[5, 500]$	$1m_{\text{AM}} + 0.62m_{\text{NIF}}$
seasalt1	1.10	0.01	1.9	$[3, 300]$	$1m_{\text{SS1}} + 0.05m_{\text{SS2}}$
seasalt2	1.10	0.1	2.0	$[0.02, 20]$	$1m_{\text{SS3}} + 0.95m_{\text{SS2}}$
organics	0.07	0.09	2.0	$[1, 1000]$	$1m_{\text{OMH}} + 0.7m_{\text{SOA}} + 0.7m_{\text{SOB}}$
soot	0.07	0.0118	2.0	$[5, 5000]$	$1m_{\text{BCH}}$

Table 2. Definition of CCN species. For each species the hygroscopicity κ as well as the median radius r_{med} and shape parameter σ of the log-normal distributions are listed. The column labelled with n reports the range of number concentrations considered; within this range, 7 geometrically spaced values are used for the Pyrcel simulations. Recipes are reported as mass mixtures m_x with x being each of the species used as CCN with definition provided in table 1; the letter H after OM and BC indicates the hydrophilic tracer.

The adiabatic parcel ascent model by Rothenberg and Wang (2016) (Pyrcel) is used to simulate activation of a heterogeneous population aerosols particles. The same parcel model has also been used by Fossum et al. (2020) to investigate the effect of large sea-salt particles to reduce the activation efficiency of sulfate CCN. Results of offline simulations are stored into a lookup table (LUT) that takes as input the number concentration of a set of pre-defined CCN species and provides number and mass activated fractions, as well as critical dry radii. Atmospheric variables for the simulated activation describe a parcel ascent with initial pressure $850\,\text{hPa}$, temperature $278\,\text{K}$ and 98% relative humidity, being lifted for $100\,\text{m}$ at $1\,\text{m/s}$. There is no dependency of the LUT on atmospheric variables other than aerosol number concentrations. Vertical velocity is known to have a relevant impact on activated particle numbers, especially in regimes with high CCN concentrations (greater than $1000\,\text{cm}^{-3}$ - so called updraught-limited) (Pruppacher and Klett, 2010; Reutter et al., 2009; Rothenberg and Wang, 2016; West et al., 2014). However, diagnosing accurate sub-grid vertical velocity and variability in a hydrostatic model with a purely-diagnostic description of turbulence can be quite a challenge; this also poses the risk of introducing significant noise in the results, rendering the identification of major sources of error, namely aerosol number concentrations, more difficult in such a first implementation of the activation scheme. Therefore, the simulations are done for every combination of number concentration for each species over 7 geometrically-spaced values, using a fixed vertical velocity of $1\,\text{m/s}$ as representative for boundary layer mixing velocities (Hogan et al., 2009), resulting in 117649 simulations. In order to keep the number of simulations low, we define a small set of 6 internally-mixed CCN species derived from aerosol species defined in Table 1, by grouping together those with similar size and hygroscopicity κ reflecting typical values from Petters and Kreidenweis (2007). The CCN species used for the offline activation simulations, as well as the definitions mapping the IFS aerosols into the CCN species (recipes) are listed in Table 2. Results of the activation process are stored in a lookup table (LUT) as critical dry activation radii, as well as corresponding activated number and mass fractions.

The LUT yields activated number fraction (a_x) for each CCN species x listed in table 2 given a mixture of particles. Such values are used to compute the amount of aerosol particles activated into droplets for each species. The number of droplets N_d is defined as the sum of the activated particles across all CCN species. The LUT can be used either online by the IFS's

https://doi.org/10.5194/egusphere-2025-3790
Preprint. Discussion started: 15 August 2025

radiation scheme to compute the r_e in liquid-phase clouds. When running the IFS with prognostic aerosol tracers, the activation scheme can also be called a second time by the wet deposition code to diagnose the activated mass fraction for each hydrophilic species. Similarly, the LUT can be invoked offline to estimate N_d from a given aerosol population.

4.2 Model data selection

Aerosol fields were produced for verification purposes from lower resolution (triangular-linear TL255, $\approx 38\ \mathrm{km}$) CAMS 1-day forecasts initialized from ECMWF reanalysis C3S (2018) v5 (ERA5) over the period 2003-2020, and stored on 16 pressure levels between $10\ \mathrm{hPa}$ and $1000\ \mathrm{hPa}$. The low vertical resolution is clearly suboptimal for the purpose of extracting accurate aerosol concentrations at cloud level; however, recycling these data allows us to get useful insights on the current state of the model climate and the potential of the tuning procedure, without needing to re-run a rather computationally-expensive simulation. We extracted from ERA5 the following meteorological fields for the period 2003-2020 on model levels: pressure (p), temperature (T), cloud cover (f), liquid (LWC) and ice (IWC) water content. Meteorological data cover the lowest 57 of 137 model levels, which correspond to up to $10\ \mathrm{km}$ altitude in the International Standard Atmosphere. For each data stream we select within each month every fifth day starting the third day of the month; for each day, we take the 00, 06, 12 and 18 UTC time-steps. All fields are interpolated on a rectangular $3^\circ \times 3^\circ$ grid.

In order to find CAMS aerosol concentrations at the cloud level, we consider only cloudy model grid-boxes, defined as those with at least 10% cloud fraction. For each column, we estimate the cloud optical thickness τ across all cloudy grid-boxes and keep only those columns for which $\tau > 4$. The formula used is:

$$\tau_k = \sum_k \left(\frac{9}{2}\pi\gamma\right)^{1/3} \frac{\mathrm{LWC}^{2/3}}{\rho_w^{2/3}} N_d^{1/3} \Delta z_k \tag{5}$$

where $\gamma = \left(\frac{r_v}{r_e}\right)^3 = 0.8$ is the ratio between mean volumetric (r_v) and effective (r_e) radius and Δz_k the geometrical thickness of the layer. N_d in equation 5 is set to $70\ \mathrm{cm}^{-3}$ over land and $170\ \mathrm{cm}^{-3}$ over sea, as estimates for N_d yielded by the wind-dependent parametrization of the IFS when the $10\ \mathrm{m}$ wind speed is $\approx 10\ \mathrm{m/s}$.

The representative cloud top level is the one for which the cumulative optical thickness computed from the top of the clouds crosses the threshold of 2 and the cloud bottom as the one for which the cumulative cloud optical thickness crosses the value of 95% of the total cloud optical thickness τ. We select warm-phase clouds by only keeping cloudy columns for which the temperature at cloud top is larger than $268\ \mathrm{K}$, and for which the ratio of ice to total cloud water is below 0.5. By doing this, we aim at selecting data points where both the model and MODIS see liquid-phase stratocumulus clouds. Note that due to the coarse resolution of the model fields ($3^\circ \times 3^\circ$), we adopted selection criteria that are more relaxed than those used for the N_d retrievals.

For a cloud layer with constant N_d profile, equation 5 yields the instantaneous relative change in τ obtained by changing N_d:

$$\frac{\mathrm{d}\tau}{\tau} = \frac{1}{3}\frac{\Delta N_d}{N_d} + \mathcal{O}\left(\left(\frac{\Delta N_d}{N_d}\right)^2\right) \approx \frac{\Delta N_d^{1/3}}{N_d^{1/3}} \tag{6}$$

https://doi.org/10.5194/egusphere-2025-3790
Preprint. Discussion started: 15 August 2025

which describes the impact of aerosols on N_d all other variables staying the same similarly to Twomey (1991). This formula assumes constant N_d distribution width, represented by the parameter γ in Equation 5. While γ has potentially a regime-dependent (Wang et al., 2023) impact on cloud albedo, as well as autoconversion of cloud water to precipitation (Liu et al., 2006), there is currently no settled knowledge about how such parametrization for γ should be used for global observations and modelling. One can incorporate the effect of γ on τ by rewriting equations 5 and 6 as functions of an effective droplet number concentration $N_e \equiv \gamma N_d$. Since typical errors in γ are estimated between 10% and 14% (see Grosvenor et al. (2018) and references therein), this would produce a relative error in τ within approximately 4%.

4.3 Optimization procedure

Aerosol mass concentration fields are interpolated at the representative cloud top level p and converted to number concentrations using equation 4. The LUT is then used offline to compute the corresponding $N_{d,\mathrm{IFS}}$ diagnostics. Such simulated values are then compared with the observed $N_{d,\mathrm{Q06}}$ using the following loss function $\mathcal{L}$:

$$\mathcal{L}(N_{d,\mathrm{IFS}}) = \left|\left| \frac{N_{d,\mathrm{IFS}}^{1/3} - N_{d,\mathrm{Q06}}^{1/3}}{\Delta \tilde{N}_{d,\mathrm{MODIS}}^{1/3}} \right|\right|_2 \tag{7}$$

$$\Delta \tilde{N}_{d,\mathrm{MODIS}}^{1/3} \equiv \max_{\mathrm{Q06,G18,BR17}} N_d^{1/3} - \min_{\mathrm{Q06,G18,BR17}} N_d^{1/3} \tag{8}$$

where the writing $N_{d,y}$ uses y to indicate either the simulated (IFS) values or one of the three sampling strategies for MODIS N_d: Q06, G18, BR17 (Gryspeerdt et al., 2022b). Here we implicitly assume that the spread across the different sampling strategies is representative of the error variance to be associated to retrievals. $||\cdots||_2$ indicates the Euclidean norm on the gridded space including weighting the grid area by the cosine of latitude.

The optimization procedure is illustrated by the flowchart in Figure 3. For each year from 2003 to 2020, $\mathcal{L}$ is evaluated by simulating N_d providing as an input to the LUT the aerosol number concentrations computed using equation 4. The procedure is repeated in a loop leaving the median radius r_{med} as a free parameter for each CCN species excluding the coarse sea salt mode (seasalt2), for which the median radius is fixed as 10 $r_{\mathrm{med,seasalt1}}$. The optimization algorithm is Nelder-Mead with free bounds. As a result, a collection of optimized median radii for each species x and year y is obtained, $r_{\mathrm{med},x,y}$. We define the optimal PSD as the one using the optimal median radius $\overline{r_{\mathrm{med},x}} \equiv \mathrm{med}_y(r_{\mathrm{med},x,y})$, i.e. the median across the 18 years of the optimized median radii.

5 Results of the N_d optimization

Table 3 reports the result of the optimization procedure for each CCN species in terms of the optimal median radius and the implied number scaling. A major aspect is the reduction in the CCN number per unit mass J of nitrate ($\times 0.36$) and organics($\times 0.19$), while J for sea salt is increased ($\times 3.25$). The optimized PSDs globally improve the simulated N_d, with a 16.5% reduction of the prior evaluation of the loss function (Equation 7) from 1.98 to 1.65. Figure 4 shows the results of the optimization procedure by comparing simulated and observed $N_d^{1/3}$ values; the reason behind this choice is that relative

https://doi.org/10.5194/egusphere-2025-3790
Preprint. Discussion started: 15 August 2025

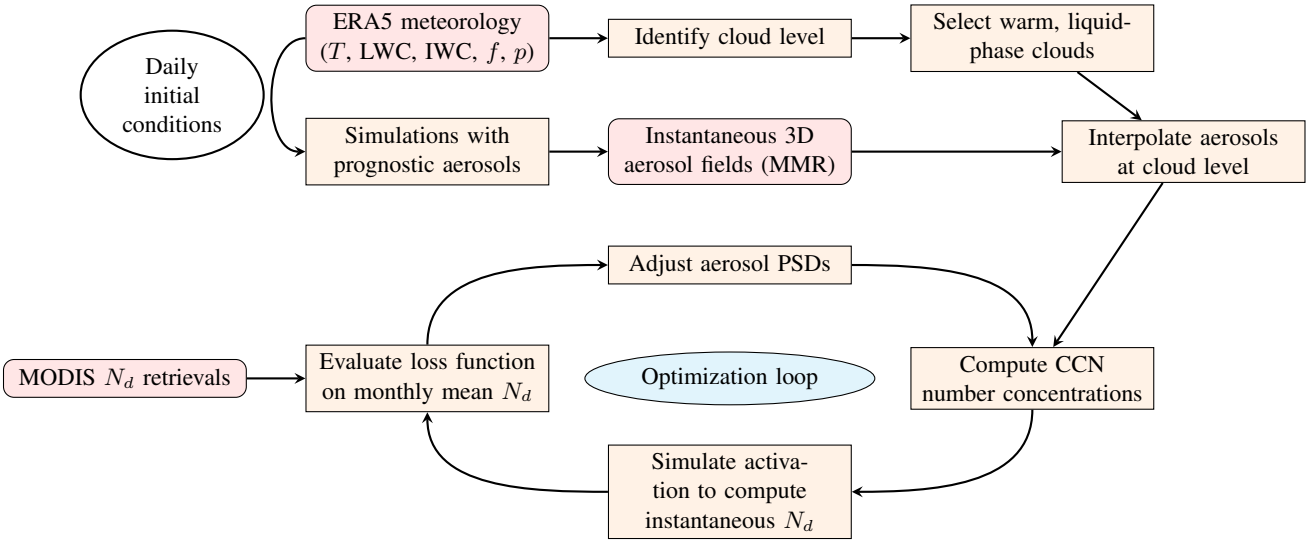

Figure 3. Flowchart illustrating the optimization procedure. This is performed over a time period of 1 year for each of the 18 years of the study. T is temperature, LWC and IWC are liquid and ice cloud water content, p is pressure, f is cloud fraction. MMR is mass mixing ratio, CCN stands for cloud condensation nuclei, N_d is cloud droplet number concentration.

CCN	initial r_{med}	InCloud r_{med} (num. ratio)	ClBase3 r_{med} (num. ratio)
sulfate	0.1100	0.091 (1.74)	0.121 (0.75)
nitrate	0.0355	0.050 (0.36)	0.047 (0.43)
seasalt1	0.1000	0.067 (3.25)	0.074 (2.45)
organics	0.0900	0.156 (0.19)	0.141 (0.26)
soot	0.0118	0.007 (5.90)	0.008 (3.67)

Table 3. Optimization result summary for each CCN species. Results are for different setups: aerosols picked at cloud level (InCloud) and 3 levels below cloud base (ClBase3) using the CCN definitions from Table 2. The table reports the optimised size-distribution median radius r_{med} in µm and the implied number ratio $J_{\text{optimized}}/J_{\text{prior}}$. For seasalt2, $r_{\text{med,seasalt2}} = 10\, r_{\text{med,seasalt1}}$, therefore the number ratio is identical to seasalt1.

295 changes in $N_d^{1/3}$ are representative of the instantaneous impact on cloud optical thickness τ, as illustrated in Equation 6. This shows that the optimization procedure significantly improves many open sea low- and mid-latitude regions characterized by typically low CCN concentrations, especially over the Pacific and the extratropical South Atlantic and Indian Ocean. Figure 4 also highlights a few regions that are recalcitrant to the optimization procedure and that are discussed more in detail below: simulated N_d are biased high over the subtropical Pacific (Hawaii) and tropical sub-Saharan Africa, and biased low over the
300 Southern Ocean.

https://doi.org/10.5194/egusphere-2025-3790
Preprint. Discussion started: 15 August 2025

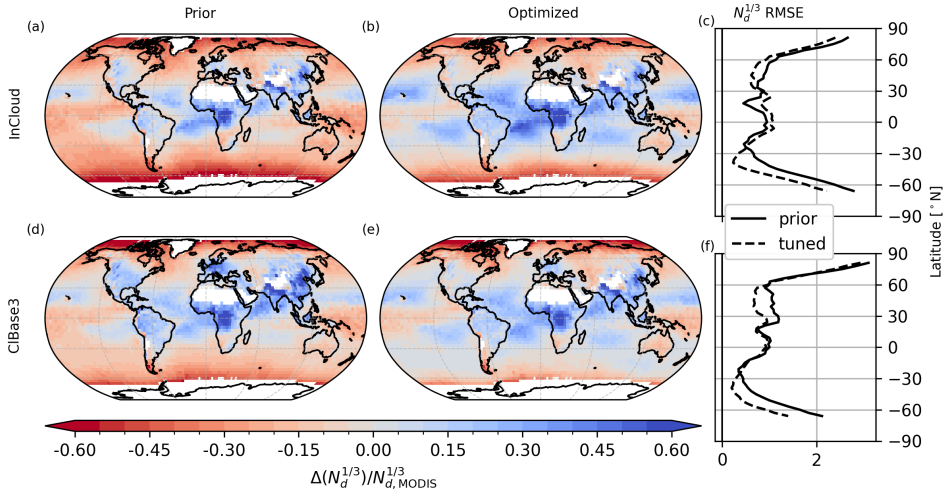

Figure 4. Impact of the optimization procedure on simulated N_d from aerosols, shown both in relative $N_d^{1/3}$ difference maps (a,b,d,e) and zonal $N_d^{1/3}$ RMSE (c, f); the figure shows results for the default tuning setup, where aerosol fields are diagnosed at cloud level, labelled as InCloud (a, b, c) and for the setup where aerosols are diagnosed three levels below cloud base, labelled as ClBase3 (d, e, f). Positive differences indicate that MODIS N_d values are higher than simulated ones. Panels (a) and (d) show prior values, i.e. before the optimization procedure; panels (b) and (e) the optimized values. Displayed data are for the mean $N_d^{1/3}$ values over the 18-year-period used for the optimization procedure.

MODIS N_d retrievals are known to suffer from an optical penetration bias due to the assumption that the spectrally-retrieved r_e values are representative of the PSD of cloud droplet at cloud top, which leads to overestimated retrieved N_d values. Grosvenor et al. (2018) quantify such penetration bias N_d for retrievals at 2.2 µm at 50% or less for clouds with $\tau_c > 4$, while Gryspeerdt et al. (2022b) found that bias-correcting retrievals improves agreement with in-situ measurements for the VOCALS and E-PEACE campaigns, targeting the subtropical stratocumulus clouds off the coasts of Peru and Namibia. Such penetration bias is within 15% when evaluated in $N_d^{1/3}$ space and typically around 10% over open sea regions within 30° latitude, which may partially explain the discrepancy between overpredicted and observed N_d values using the prior definitions.

At latitudes higher than 60°N and 45°S our method struggles at getting N_d high enough compared with observations. MODIS cloud retrievals are known to suffer from viewing geometry errors with large satellite and solar zenith angles (Maddux et al., 2010; Grosvenor and Wood, 2014), which could in principle degrade high latitude observations; such effects are included in one of the sampling strategies and contribute to defining the error bars that we associated with the MODIS observations. According to Gryspeerdt et al. (2022b), at latitudes larger than 60° such errors are positive and small, on average within $16\ \mathrm{cm}^{-3}$, which could still be relevant in relatively pristine regions over sea, with typical retrieved N_d values between $75\ \mathrm{cm}^{-3}$ and $100\ \mathrm{cm}^{-3}$. However, this only partially explains the low bias in simulated N_d at high latitudes.

https://doi.org/10.5194/egusphere-2025-3790
Preprint. Discussion started: 15 August 2025

Figure 5 shows how using the optimized PSDs would impact simulated AOD, with mass concentrations staying constant. On a zonal mean, the new definitions for sea salt and nitrates tend to slightly increase AOD, with a larger relative impact at mid- and high latitudes in the Southern hemisphere. Despite the drastic change in simulated CCN number concentrations from using the optimized PSDs, the mean and local impact (not shown) on total visible AOD remains within a 10% range from the current definitions. Once again, this shows that aerosol PSDs are not well constrained by the need to correctly simulate their direct effect. Simulated AE is potentially more deeply affected by re-defined PSD, but for this scenario the impact is generally neutral. Degradation in simulated AE is verified between 10°N and 45°N and is due to the combined signal of SS, SU, NI aerosol and advected Mineral Dust over the Atlantic.

5.1 Tropical Nd

Using the default CAMS definitions leads to globally too low N_d associated with sulfate CCN over oceans. The optimization procedure results in a reduced PSD r_{med} for this species from 0.11 µm to 0.09 µm. Interestingly, the PSD for Sulfate aerosol was updated in IFS-COMPO CY49R1 $r_{\text{med}} = 0.0355$ µm and $\sigma = 2.0$. Indeed, the CY48R1 PSD definitions tended to overestimate Sulfate-associated CCN numbers by a factor 2.7 (not shown), while these are underestimated by a factor $1/1.74 = 0.57$ with the new PSD definitions (see Table 3). Generally speaking, the IFS-COMPO aerosol scheme does not represent any change in aerosols PSD over time, and for binned species like SS and DU, no transfer of mass between bins is allowed (ECMWF, 2024). However, mass transfer from Aitken ($r \approx 0.04$ µm) to accumulation ($r \approx 0.1$ µm) mode has been assessed by observations in tropical marine regions, and is likely driven by the incorporation of soluble aerosols in non-precipitating boundary-layer clouds (Hoppel et al., 1990). Both Aitken and accumulalation modes for sulfates have been for long time deployed in the Met Office Unified Model (Jones et al., 2001), with a typical local mass apportionment between Aitken and accumulation mode by 1:10 (Mulcahy et al., 2014). The general underestimation of N_d over the oceans might be therefore indicating differences in sulfate PSD in regions dominated either by oceanic or anthropogenic emissions. If this is the case, it might be beneficial to introduce an additional aerosol mode, either for sulfates or internally-mixed aerosol, to more precisely represent the spectrum of sulfates PSDs.

Optimal PSDs for nitrate and organics CCNs (see Table 3) are systematically shifted toward larger particle sizes relative to the prior definitions, respectively resulting in number reduction by factors 0.36 and 0.19. Such results for organics are due to OM aerosols at cloud level peaking over sub-Saharan Africa, Northern India, China and South-East Asia (not shown), which are all regions where N_d tends to be overpredicted using the default definitions. S However, simulated N_d are degraded over sub-Saharan Africa and the tropical South Atlantic Ocean in the optimized setup. These results reflect the frequent co-presence of sulfates, soot and nitrates CCN whenever there are organics, so that simultaneous optimization might result in local degradation in order to improve the global metric.

We are aware that the IFS wet scavenging scheme might be underestimating the aerosol mass fraction scavenged by precipitation in liquid clouds, which may result in overestimated aerosol mass concentrations and, in turn, simulated N_d. This is due to the fact that the fixed scavenging coefficients (between 0.7 and 0.9) for hydrophilic species are significantly lower than the typical mass activation rates close to unity provided by the activation scheme. We quantified the relative change in aerosol

https://doi.org/10.5194/egusphere-2025-3790
Preprint. Discussion started: 15 August 2025

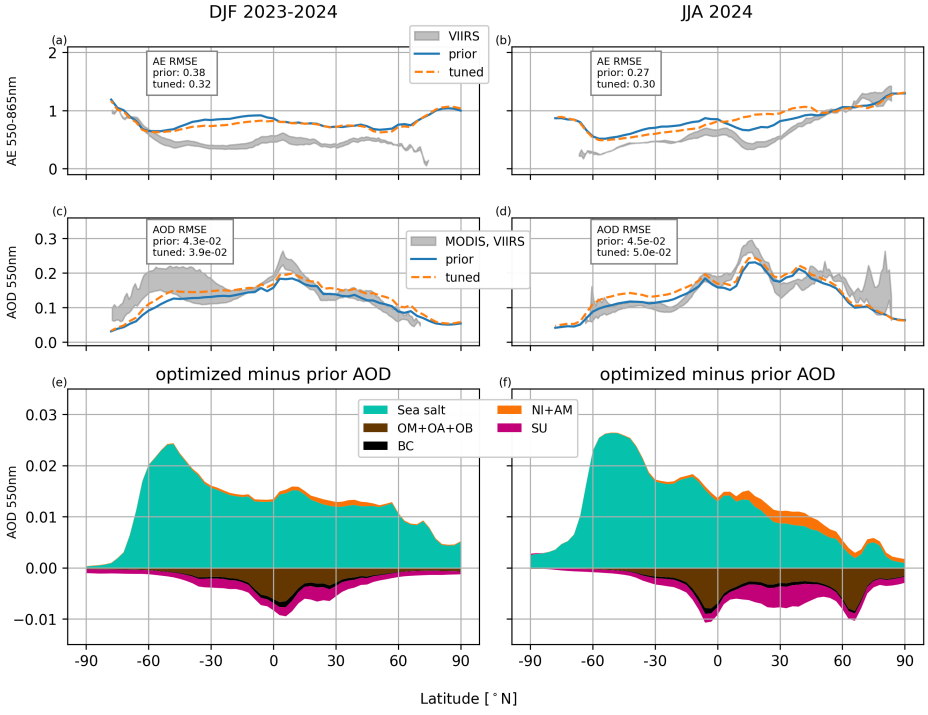

Figure 5. Simulated aerosol optical properties for the DJF 2023-2024 (a,c,e) and JJA 2024 (b,d,f) seasons from Mie computations using the prior IFS aerosol definitions from Table 1 (prior), and using the optimized median radii for in-cloud N_d from Table 3 (tuned). Panels (a,b) show the zonal mean AE ($550 - 865$ nm), (c,d) zonal mean 550 nm AOD. RMSE in space for the seasonal mean values of simulated AE and AOD is also reported. The gray shadings display the range of observed zonal mean values from VIIRS (NOAA20 and SNPP) for the AE, and including also MODIS (Aqua and Terra) for the AOD. The bottom panels (e,f) show the tuned-minus-prior difference in AOD as a breakdown for the aerosol species used during the tuning procedure.

mass burdens obtained by diagnosing the scavenging coefficients from the activation scheme lies within 5% for SS and AM, within 15% for SU, NI, SOA and SOB, and within 18% for OM (more details are given in Appendix C). Errors in simulated aerosol burdens for these species are therefore unable to explain the generally-low N_d values prior to tuning, and insufficient to address the large overestimation over tropical Africa. Moreover, producing the required number by scaling mass would linearly impact AOD, which would be directly observable, especially at tropical latitudes, where the model rarely overestimates AOD, especially over sea (see discussion below).

We selected six regions to better investigate remaining errors after the optimization procedure: over the north tropical Pacific (NTP), southern equatorial Atlantic (SET), north tropical Africa (NTA), central Africa (CAF), Europe (EUR) and India (IND). Their extents are reported in Figure 6. All defined regions except Europe are characterized by a high N_d bias ranging from 15% (NTP) to more than 60% in relative $N_d^{1/3}$ difference (see Figure 4). The mean simulated and observed monthly $N_d^{1/3}$ for a seleciton of regions are illustrated in Figure 7; these include the NTA, CAF and MAT regions of overestimation, as well

https://doi.org/10.5194/egusphere-2025-3790
Preprint. Discussion started: 15 August 2025

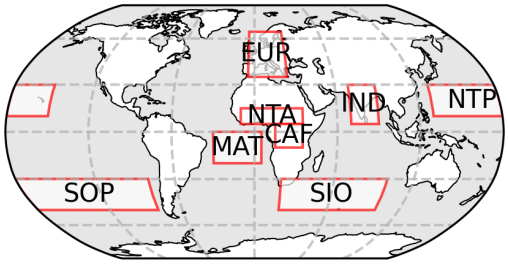

Figure 6. Regions defined for the analysis of residual N_d biases in the optimized setup. Labels indicate North Tropical Africa (NTA, 350°E-35°E, 5°N-15°N), Central Africa (CAF, 15°E-35°E, -10°N-5°N), Southern Equatorial Atlantic (MAT, 330°E-5°E, -20°N-0°N), India (IND, 70°E-90°E, 5°N-30°N), North Tropical Pacific (NTP, 130°E-210°E, 10°N-30°N) and Europe (EUR, 355°E-25°E, 35°N-65°N)

as the NTP, SOP and SIO regions, where the optimization procedure had a neutral to decisively positive impact. For the NTP region, simulated N_d for both prior and optimized setup are within the uncertainty range spanned by the observations, with the prior located at the lower end and the optimized values at the upper end; the residual difference between the simulated N_d values and those provided by the tuning target is large (up to 20%) in terms of instantaneous impact on cloud reflectivity. Such large impact is due both to the relatively-clean conditions of the NTP region and the magnitude of the uncertainty range, loosening the constraint for the representation of the Twomey effect in this region. For the NTA, CAF and SEA regions instead, the positive bias is located out of the uncertainty bars and has a rather strong seasonality: the bias peaks during the period November-March for the NTA region, December-February and June-September for the CAF region, August-October for the SEA region. The aerosol speciation for these three regions indicate that between 60% and 90% of simulated N_d values are due to activation of organics and soot CCN (not shown). In the IFS-COMPO, carbonaceous aerosols emissions from observed wildfires are represented via the Global Fire Assimilation System (GFAS), that provides daily inventories of emissions by assimilating fire radiant power from satellite observations (Kaiser et al., 2012). Figure 8 shows that, for the CAF and NTA regions, wildfire carbon-containing aerosol emissions from GFAS are a very good predictor of errors in simulated N_d values on a monthly basis, respectively with a normalized covariance of 0.77 and 0.88, which narrows down our investigation to the regional wildfire seasons in Africa. The scatter plots report also the examples of the IND and EUR regions, where wildfires are instead a rather weak predictor of N_d errors. However, to our knowledge, GFAS wildfire emissions in the NTA and CAF regions are unlikely to suffer from so strong a positive bias able to explain a four- to five-fold error in simulated N_d as illustrated in Figure 7.

Figure 9 shows aerosol size spectra as observed by AERONET and simulated from CAMS aerosols for sites located close to the NTA and CAF regions. The plotted quantity is the PSD of the spherical geometrical cross-section:

$$\frac{\mathrm{d}\sigma}{\mathrm{d}lnr} = \pi r^2 \, r \frac{\mathrm{d}N}{\mathrm{d}r} \tag{9}$$

https://doi.org/10.5194/egusphere-2025-3790
Preprint. Discussion started: 15 August 2025

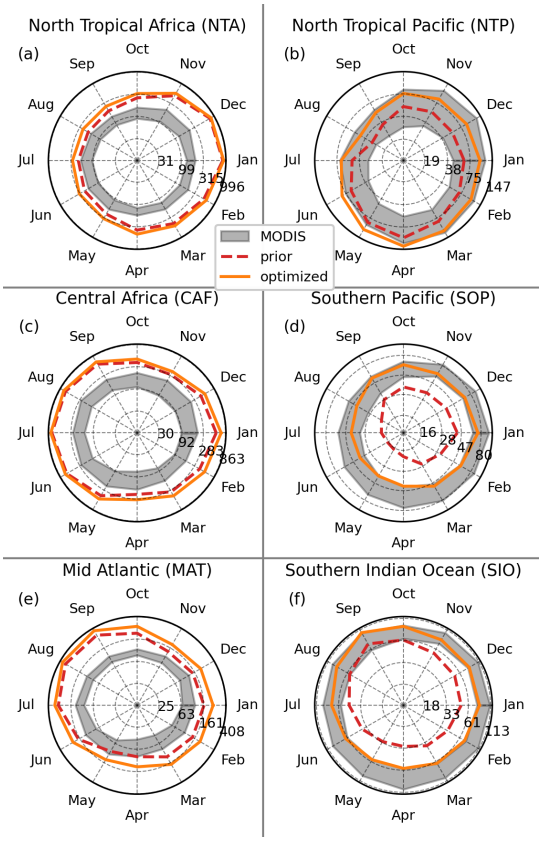

Figure 7. Simulated and observed N_d for a selection of regions (see definitions in Figure 6 for NTA, NTP, CAF, SOP, MAT, SIO). For each month, data are averaged over the 2003-2020 period. Shadings indicate the range of mean values spanned by the N_d retrieval datasets as in Equation 8.

weighted by the Mie extinction efficiency $Q_{\text{eff}}(r)$ at 550 nm for a real refractive index $m = 1.3$. By doing this, the area below the curves is an indicator of the optical depth of the entire aerosol column obtainable from such spectra. The flattening spectrum at particle radii smaller than ≈ 0.1 µm is due to the r^6 dependency of the extinction efficiency in the Rayleigh scattering regime. While these finer particles are the largest contributors to CCN numbers, they are the least detected from sun photometers, which poses an important limitation to using AERONET size spectra to validate CCN. Selected stations north and south of the equator present a peak in AOD respectively during the DJF and JJA season, consistently with the regional wildfire season. The most articulated size spectra are found for the stations north of the equator, where three modal peaks are found: at 0.1 µm, 0.6 µm and 2 µm. The two coarser peaks are also present in simulated values and are produced by Mineral Dust likely advected by Northerly trade wind systems such as the Harmattan in Western Africa. Interestingly, the finest peak produced by the model is found around 0.3 µm (associated to OM aerosol), while it is located at less than 0.2 µm or even 0.1 µm in the AERONET data.

https://doi.org/10.5194/egusphere-2025-3790
Preprint. Discussion started: 15 August 2025

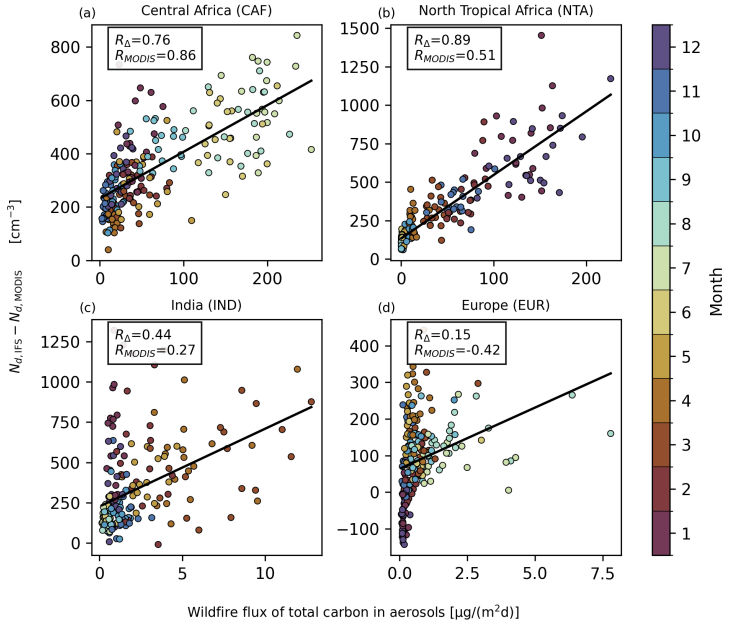

Figure 8. Scatter plot of wildfire flux of total carbon in aerosols from the GFAS system and differences in simulated monthly N_d. Points indicate monthly mean values for each year between 2003 and 2020.

Despite the overall number of particles being generally underestimated by the model, the overall area below the graph in the $r < 1$ µm regime is in fairly good agreement between model and observations.

It is not straightforward to infer how shifting the carbonaceous aerosol population toward (finer) observed modes would impact simulated N_d. In fact, particles with radii < 15 nm are weakly activated into cloud droplets, especially when characterized by low hygroscopicity, as in the case of soot. By representing BC with the same PSD as pristine soot, the activation scheme might be overestimating the number of available BC particles. In fact, this setup implicitly neglects the property of soot to form large chain-like clusters, which results in a reduction of the effective number of separate particles available for activation. At the same time, the representation used in the activation scheme is expected to induce underestimated black carbon activated mass fraction by neglecting the property of such clusters to grow into larger structures and incorporate highly hydrophilic salt crystals like sulfates. Despite this uncertain representation, adding BC to the tuning procedure has a neutral-to-positive impact on results. For carbon CCN defined as in Table 2, we assessed a median simulated number activation rate around 0.5%. If we considered "realistic" aged BC in the form of aggregates of hundreds to thousands monomers oftentimes incorporating organics and sulfates crystals, this would imply a total amount of aggregates which is lower by two to three orders of magnitude, but which readily activate due to internal mixing with larger and more hydrophilic particles. This means that the total number of activated nuclei from BC particles would not be too far from the one simulated with the current setup. Therefore, even if for the wrong reason, the activation scheme might be providing fairly-realistic orders of magnitude for activated aged BC CCN.

https://doi.org/10.5194/egusphere-2025-3790
Preprint. Discussion started: 15 August 2025

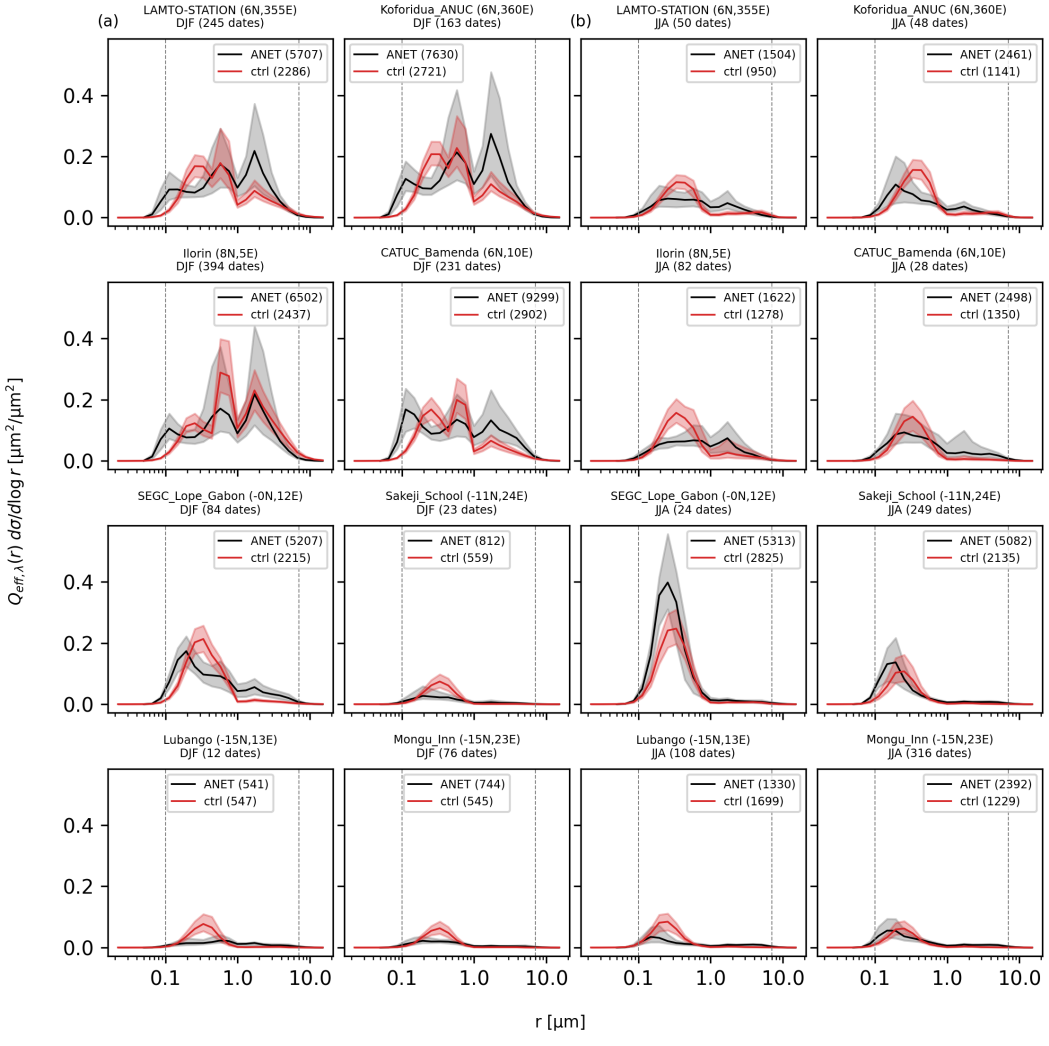

Figure 9. Aerosol size spectra for several low-latitude AERONET sites during the DJF and JJA season. Sites are ordered from top to bottom by decreasing latitude. Plotted quantity is defined by Equation 9, integrated over a whole atmospheric column. For each panel, lines correspond to the AERONET inversion retrieval (ANET) and the IFS (ctrl). Together with each label in the legends are reported the total column particle numbers for the domain $[0.09\,\mu m, 2\,\mu m]$; the unit $10^{-3}\ \mu m^{-2}$ or, equivalently, the mean number concentration expressed in cm^{-3} for a 1 km-deep layer with the same total-column amount of particles.

https://doi.org/10.5194/egusphere-2025-3790
Preprint. Discussion started: 15 August 2025

However, it is unclear whether this is enough to catch the variability in particle shape and size of real carbonaceous particles. Conversely, if we consider the possibility that the PSD for hydrophobic BC overestimates dispersion and/or the median particle size, this would result in an underestimation of the total amount of particles in the $r < 0.1\ \mu\mathrm{m}$ regime, which would in principle explain the discrepancies in the size spectra in Figure 9. It is also key for the model to accurately simulate the emission category of carbonaceous aerosol, either soot or other organic compounds, as well as the conversion timescales from hydrophobic (pristine) to hydrophilic (aged) BC. Possible sources of error are a misrepresentation of the wildfire type (Forkel et al., 2025) and the associated smoke plume, with repercussions on the vertical aerosol profile and efficiency of ageing processes.

5.2 Missing high-latitude CCNs

Very few fine sea salt particles are found at cloud level in our simulations. Figure 10 (a) shows that, during the optimization procedure, these play an overall negligible role as CCN providers, especially in high-latitude, stormy, open ocean regions regularly covered by boundary-layer stratocumulus clouds like the Southern Ocean. At lower latitudes, mixing of sea-salt transport across boundary layer is facilitated by convective updraughts resulting in somewhat higher values at cloud level. In principle, low numbers concentrations agree with the understanding that sea-spray is typically a provider of CCN of secondary importance (e.g. McFarquhar et al., 2021); however coarse sea salt components are known to compete during activation with less hygroscopic particles (Fossum et al., 2020), impacting cloud optical thickness inversely to their concentration. Realistic aerosol profiles are therefore key to quantify such deactivation effect in the model. Our setup also displays negligible suppression effect (within 3% in relative τ change, not shown), mostly indicating absence of coarse sea salt particles at cloud level.

Figure 10 a) shows that less than $30\ \mathrm{cm}^{-3}$ sea salt particles are found at mid- and higher latitudes at the cloud representative level during the tuning procedure. In many of these regions, like the Southern Ocean (SO), mixing is mostly driven by stormy weather. Multiple aircraft and ship campaigns observed SO clouds to be oftentimes in a mixed phase of super-cooled liquid water and ice crystals (McFarquhar et al., 2021). Figure 4 b) shows that diagnosing aerosols below cloud base, instead of inside the cloud, results in significantly higher numbers at mid- and high latitudes. This approach relies on the assumption that the cloud and the underlying boundary layer are well mixed, which is reasonable for stratocumulus clouds. This improves the output of the optimization procedure especially over the Southern Ocean (see figure 4 c, d) reducing the value of the loss function (see equation 7) at the end of the tuning for all the 18y period by 13%. From this result, we drew three main messages: firstly, sea salt profiles indicate weakly-superposing boundary layers between clouds and aerosols, with these latter sharply skewed toward the below-cloud space; secondly, such in-cloud values are so low that the tuning procedure is unable to retrieve the beneficial signal found instead below cloud base, indicating a very strong reduction of aerosols inside the cloud; thirdly, the too-low simulated N_d can potentially be tracked down to scarcity of CCN at cloud level.

6 Testing changes in the aerosol wet-scavenging scheme

In order to investigate the low CCN concentrations at cloud level we collected diagnostics of in-cloud (rain-out, IN-SC) and below-cloud (wash-out, BC-SC) wet scavenging (SC) as well as release by precipitation evaporation (EV). These confirmed

https://doi.org/10.5194/egusphere-2025-3790
Preprint. Discussion started: 15 August 2025

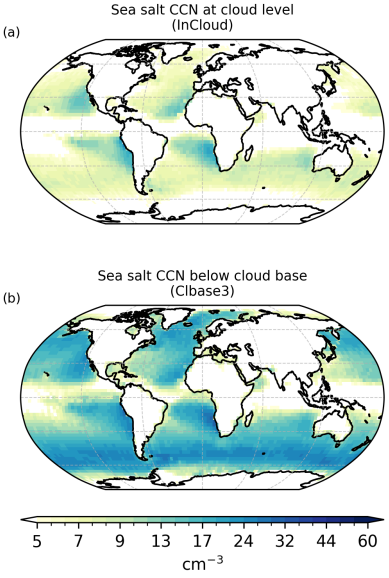

Figure 10. N_d from sea salt activation diagnosed during the offline tuning procedure (mean for the entire 2003-2020 period). Values are shown for the aerosol found at cloud level (InCloud, a) and three model levels below cloud base (ClBase3, b).

our expectation that IN-SC from large-scale precipitation dominates the removal of SU and SS, while EV is significant in modulating tropical and subtropical aerosol mass budgets. For latitudes larger than $55°$ and along the intertropical convergence zone (ITCZ) the residence time due to IN-SC of an entire column of SS particles is estimated around 10 hours, for SU is around 18 hours (not shown), impacts on total budgets for hydrophilic species on time scales below 1 day. Then, we performed a short (2 days) sensitivity experiment with switched off IN-SC for SS, yielding homogeneously distributed aerosols between cloud base and top (not shown). While this setup improved profiles, it also obviously results in non-realistically high concentrations overall, due to the impossibility to remove SS from the atmosphere.

We decided to focus on the IN-SC parametrization for precipitating mixed-phase (MP) clouds, where supercooled liquid and ice water coexist at temperature between $-38\,°\mathrm{C}$ and $0\,°\mathrm{C}$. For these clouds, the air is overall supersaturated with respect to ice but sub-saturated with respect to water and ice crystal growth occurs through the Wegener-Bergeron-Findeisen (WBF) process by deposition of water vapor while cloud droplets evaporate (Pruppacher and Klett, 2010). From the standpoint of aerosols, this implies evaporation of activated CCN into interstitial cloud space, therefore limiting the efficiency of aerosol removal by precipitation compared to warm-phase clouds, where only liquid water is present (Verheggen et al., 2007). Released aerosols incorporate information on micro-physical cloud processes occurred prior to evaporation, e.g. collection, collision-coalescence or nucleation, and are expected to be internal mixtures with size generally larger than the originally activated CCN

https://doi.org/10.5194/egusphere-2025-3790
Preprint. Discussion started: 15 August 2025

particles (Hoose et al., 2008). Within the IFS single-moment cloud scheme no memory of cloud particle numbers is preserved, necessarily limiting the realism of a representation of the impact of the WBF process on aerosol number concentrations. Based on observations at one station in the Swiss alps, Verheggen et al. (2007) produced two parametrization to modulate activation efficiency in mixed-phase clouds. The first one defines a modulating factor function of cloud temperature, here referred to as $\zeta(T) \in [0,1]$, to scale the activated number fraction of aerosol particles with diameter larger than $100\,\mathrm{nm}$; the second one defines the same modulating factor but as a function of ice water ratio $IWR \equiv IWC/(IWC + LWC)$, $\zeta(IWR)$. The same parametrization has been deployed in other global transport models leading in increased black carbon burdens at high latitudes that better matched observations from the HIPPO aircraft campaign (Liu and Matsui, 2021). The IFS IN-SC scheme diagnoses the aerosol removal rates by relating formation of snow to the cloud ice content and formation of rain to the cloud liquid content. Aerosol activated mass fraction is then scaled by $\zeta(T)$ whenever snow is produced (ECMWF, 2024).

We present here results about the two following experiments with modified IN-SC parametrization in the following ways:

- **IWR2** uses $\zeta(\mathrm{IWR})$ to scale activated mass fraction both when either snow or rain is produced;
- **IWR5** adds the following to the setup of IWR2:
  1. diagnose the aerosol removal rate using the ratio between the precipitation formation and the total cloud condensate instead of treating the ice and liquid phases separately;
  2. $\zeta = 1$ at riming regimes, identified with T between $261\,\mathrm{K}$ and $265\,\mathrm{K}$ when $\mathrm{LWC} > 1\,\mathrm{g/m^3}$ following Qi et al. (2017);
  3. set mass activation rates to 1 for all hydrophilic species except BC, consistently with numbers provided by the activation scheme;
  4. balance opposite-sign formation rates of rain and snow to exclude freezing and melting from the IN-SC routine;
  5. implement a bug-fix for overestimated sedimentation of medium and coarse sea-salt dry deposition.

Figure 11 shows a cross-section of the model for a case-study on September 17, 2024, using a 10-days spin-up time; the number mixing ratios of CCN in the control simulation drops to values below $30\,\mathrm{cm^{-3}}$ in high-latitude clouds simulated over the SO forming snow precipitation consistently to what stated above about the sea salt CCN diagnostics in- and below the cloud. The IWR5 setup increases CCN numbers found inside the cloud up to about $100\,\mathrm{cm^{-3}}$, providing a background of CCN compatible with higher and more realistic N_d values.

We also tested the IWR2 and IWR5 setups by performing CAMS daily forecasts over the boreal winter (DJF) 2023-2024 and boreal summer (JJA) 2024 seasons. These simulations use meteorological initial conditions from ERA5 analyses, while chemical and aerosol tracers are restored from the previous forecast day at valid time +24h, thus leaving them free to evolve. These setups use a spin-up time of 1 month to ensure that tracers are aligned with the climate of the model.

Figure 12 shows a comparison between column-integrated aerosol size spectra from the model and the corresponding AERONET inversion product Dubovik and King (2000) for the stations at the highest latitudes in the southern (DJF season) and northern (JJA season) hemisphere. The same figure reports total column numbers obtained by integrating $\frac{\mathrm{d}N}{\mathrm{d}r}$ over the

https://doi.org/10.5194/egusphere-2025-3790
Preprint. Discussion started: 15 August 2025

domain $r \in [0.1\ \mu\mathrm{m}, 5\ \mu\mathrm{m}]$. The reason for restricting the integration domain is in the progressively lower sensitivity and larger errors in the AERONET product towards the tails of the distribution as reported in (Dubovik and King, 2000). This constitutes an important limitation to the validation of aerosol number concentrations using measurements from sun-photometers: in fact, despite a large majority of particles are found at radii smaller than $0.1\ \mu\mathrm{m}$, these interact very weakly with visible wavelengths, due to a decline in extinction efficiency $Q(r) \propto r^6$ in the Rayleigh regime.

For all stations at latitudes higher than 60N and 60S the control simulation has lower particle counts within the integration domain, while IWR2 and IWR5 result in significantly increased particle numbers resulting in better agreements with values from AERONET. Figure 13 shows that, in terms of AOD, the control simulation tends to be biased high with respect to AERONET. The model also tends to produce systematically low AE values, which points at an overestimate of AOD contribution from coarse aerosols. The optical thickness in the simulated spectra is provided by modes shifted to larger sizes compared with AERONET; these larger modes are also amplified in IWR2 and IWR5 that, despite providing better agreement in particle numbers, tend to be biased high in AOD against AERONET. It must be noted that this contrasts with validation against satellite AOD. In fact, Figure 13 shows that at high latitudes the model's AOD tends to be biased low compared to MODIS, and biased high compared to AERONET. Such discrepancy between MODIS and AERONET AOD at high latitudes is consistent with the analysis reported in Gupta et al. (2018). The IWR2 and IWR5 experiments have systematically higher AOD at high latitudes, but tend to have systematically lower AE than AERONET, which indicates too large contribution to AOD by coarse mode aerosols. Better understanding of such discrepancies is limited by the relative scarcity of observations from sun photometers especially in the Southern Hemisphere, and the absence of observations over sea.

Figure 14 shows the top of the atmosphere (TOA) biases in SW fluxes against CERES for the DJF 2023-2024 season. The panels show results of a control simulation, where cloud N_d and r_e are computed by the IFS wind-dependent parametrization and three simulations where cloud N_d values are diagnosed from aerosol fields by the activation scheme, all labeled as "InCloud". Of the three InCloud simulations, one uses the default wet scavenging parametrization, the other two use the IWR2 and the IWR5 setup. Note that the all setups use the same aerosol PSD definitions resulting from the InCloud optimization discussed in section 5. Like many global models (Bodas-Salcedo et al., 2014), the IFS reflects too little SW radiation over the Southern Ocean, and this is consistently illustrated by the control simulation. InCloud displays a strong degradation by up to $20\ \mathrm{W/m^2}$ (see figure 14) of the TOA SW bias over the SO, associated with decreased optical thickness of clouds, consistently with the indication of too low N_d values at these latitudes. Such degradation is strongly reduced by InCloud-IWR2 and totally removed by InCloud-IWR5, which has an overall neutral impact over the SO.

Figure 15 shows the zonal mean (only over sea) AOD RMSE against MODIS (M3 monthly) of the experimental setups. The largest absolute impact of IWR2 and IWR5 is found at the high latitudes toward increasing aerosol burdens; these coincide to regions where the tuning procedure struggled the most at producing large enough N_d values. Over the SO the two setups set a decisive improvement against MODIS, with biases being almost eliminated during the JJA season between latitudes 45S and 60S in the IWR5 setup. In the winter hemisphere, IWR2 and IWR5 seem to produce too large AOD at latitudes as low as 45N and 30S, indicating that the system might be lacking the right seasonal cycle of emissions over the oceans at high latitudes. A possible explanation could be that the IFS, despite linking SU production to the oxidation of available dimethyl sulfide (DMS),

https://doi.org/10.5194/egusphere-2025-3790
Preprint. Discussion started: 15 August 2025

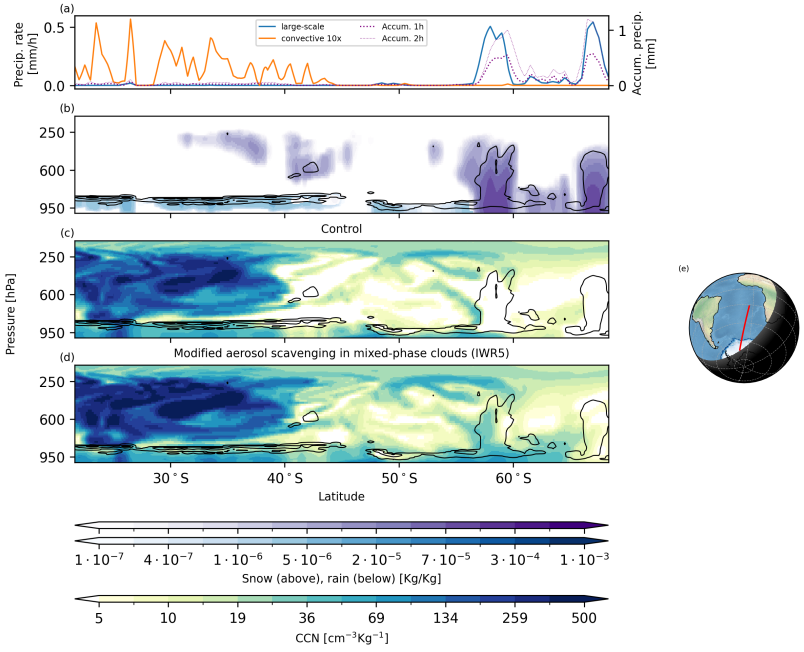

Figure 11. Model cross-section over the Atlantic and Southern Ocean on 18 September 2024, 15:43 UTC. From top to bottom, the first two plots show total precipitation (snow and rain) at surface (a) and vertical cross-section of precipitation (b); the two plots at the bottom show the vertical cross-section of CCN number mixing ratios (sulfates, fine sea salt, organic matter) in the control simulation (c) and for the modified wet scavenging for mixed-phase clouds (d). Contours in panels b, c and d indicate total (liquid plus ice) cloud water mixing ratio, start at $2 \cdot 10^{-5}$ and are spaced by $5 \cdot 10^{-5}$. The track location on the globe is displayed on the right (e) and corresponds to EarthCare segment labelled 01752F.

has no representation of sea-borne marine organic aerosols. These are likely linked to photosynthetic activity of phytoplanktons (Sellegri et al., 2024) and are found to significantly contribute to spatio-temporal variability of cloud N_d (McCoy et al., 2015). Therefore, considering sea spray as only SS containing might result in an overestimated burden of SS, with boundary layer aerosols lacking the correct seasonal cycle.

7 Summary, outlook and conclusions

In this study we showed that aerosol-cloud interactions (ACI) in a weather model can provide novel constraints on modelled aerosol processes. To do this, we introduced a lightweight aerosol activation scheme into the ECMWF Integrated Forecasting System (IFS) used to implement the Copernicus Atmosphere Monitoring Service (CAMS). Then, we optimized droplet number concentrations (N_d) from CAMS aerosols using an 18-year-long series of MODIS N_d retrievals. We finally combined the results of the optimization procedure with extensive observations of aerosols and all-sky radiative fluxes to evaluate other-

https://doi.org/10.5194/egusphere-2025-3790
Preprint. Discussion started: 15 August 2025

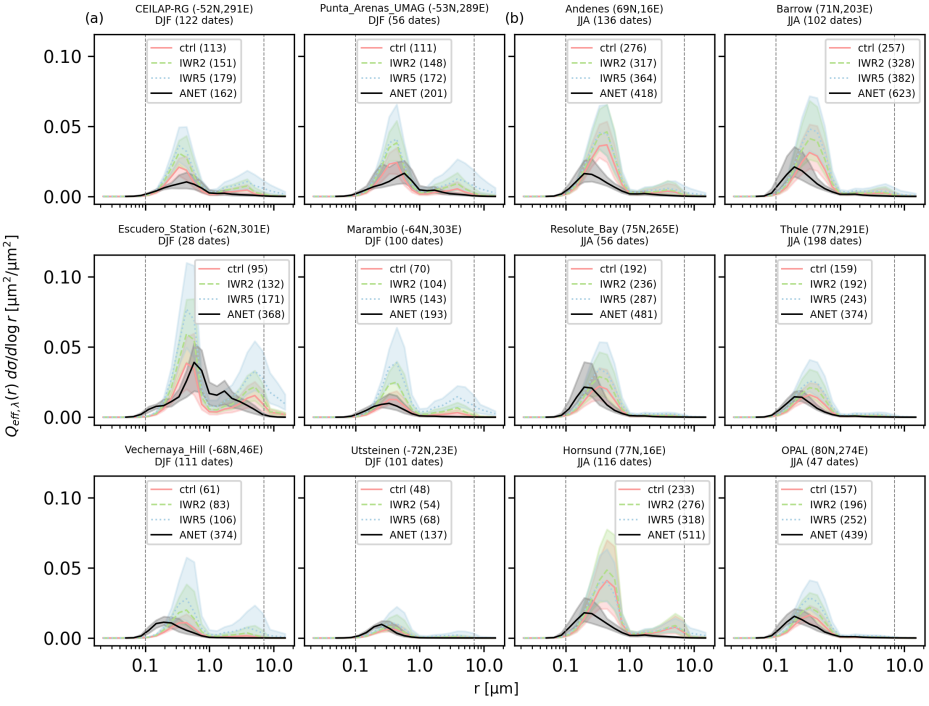

Figure 12. Aerosol size spectra at a selection of high-latitude AERONET locations, respectively for the southern (group a, season DJF) and northern (groub b, season JJA) hemisphere. For each panel are also reported values for the two changed mixed-phase clouds wet-scavenging parametrization (IWR2) and (IWR5). Sites are ordered from top to bottom by increasing (absolute) latitude.

wise poorly-observed aerosol processes. As a result, we identified possible issues associated with wildfire emissions, and we effectively evaluated an upgrade of the wet-scavenging parametrization of the model.

The optimization procedure based on satellite observations corrects the prior model CCN number concentrations over the tropics by decreasing the PSD median radius for sulfates, while increasing it for organic matter and nitrates. Despite the substantial effect in number concentrations (up to a factor five), the implied change in visible AOD is negligible. Using optimal PSDs highlights a few regions that appear more recalcitrant to the optimization procedure. The procedure failed also to correct the too low high-latitude CCN number concentrations. Results improved when the aerosols mixing ratios were diagnosed below cloud base, due to the steeply-declining profile of sea salt aerosols at the base of mixed-phase clouds.

We could track down a macroscopic N_d overestimation (by a factor four to five) over north tropical and central Africa to the carbonaceous aerosol emissions during the wildfire season. Moreover, data from AERONET stations suggest that the model is not generally overpredicting AOD, but rather overestimating the typical particle size of the finer ($< 0.5\ \mu\mathrm{m}$) carbonaceous aerosol. We suggest that this hints at potential improvements of the description of pristine and aged aerosols from wildfires,

https://doi.org/10.5194/egusphere-2025-3790
Preprint. Discussion started: 15 August 2025

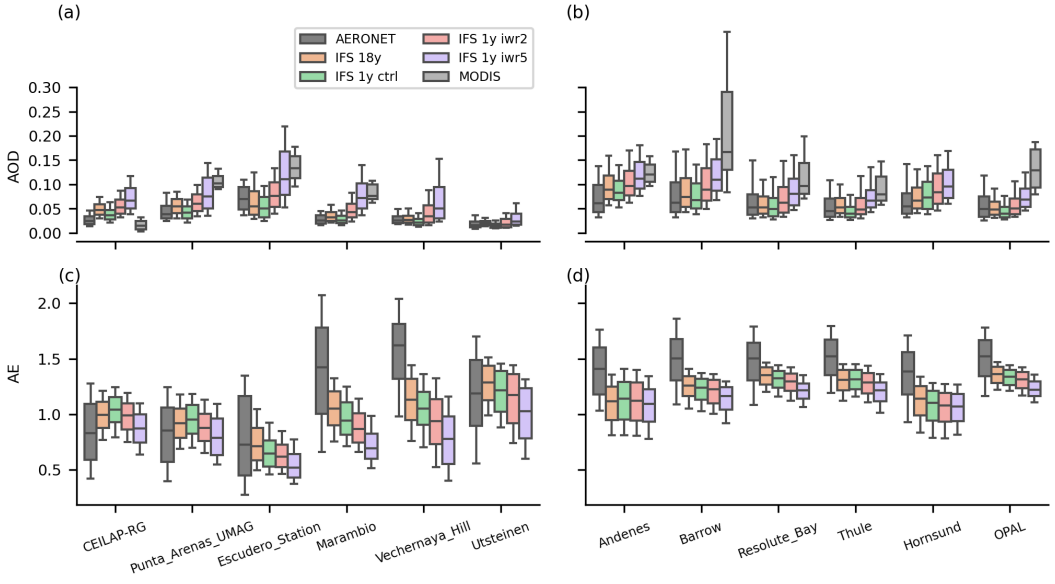

Figure 13. Boxplots of AOD (a,b) and Angstrom exponent (c,d) for the high-latitude AERONET sites in the southern (a,c) and northern (b,d) hemisphere, as shown in figure 12. MODIS data (Aqua and Terra means) are present in the AOD panels (a,b) only when enough valid retrieved pixels are available.

including the possibility to represent smaller pristine soot particles and larger, eventually internally-mixed aged aerosol. Possible future investigations could concern the accuracy of the described wildfire regime, as well as smoke plume properties, with downstream impact on carbonaceous aerosol vertical profiles and ageing timescales.

To illustrate the diagnostic potential of ACI for constraining CAMS aerosol processes, we experimented two model versions that introduced modifications of the wet scavenging scheme. These target process representations that led to overestimated scavenged aerosol mass fraction in mixed-phase clouds. These changes improved the number mixing ratio of CCN inside mixed-phase clouds, as well as the simulated total-column aerosol particle numbers and AOD during the austral summer. This resulted in successful elimination of the top-of-the-atmosphere broadband shortwave bias over the Southern Ocean introduced by using the activation scheme with the CAMS aerosols in the current model version.

CAMS aerosols can overall produce realistic CCN number concentrations and, in turn, N_d values, if number-to-mass conversion factors are calculated from optimized PSDs. The optimization procedure also offers valuable information on number concentrations of CAMS aerosols, that would otherwise be weakly constrained by traditional AOD observations. The optimized PSDs showed that the CAMS aerosols description over tropical and mid-latitudes seas could significantly benefit from the introduction of an accumulation mode to represent aging of sulfate, nitrate and organic matter aerosol species. In order to produce realistic N_d values over the Southern Ocean, the CAMS aerosol need to improve air composition at cloud level, that we show might be done with a more sophisticated parametrization of wet scavenging in mixed-phase clouds. Such modifications also increase AOD over sea at high latitudes, which is beneficial in the summer hemisphere, but detrimental in the

https://doi.org/10.5194/egusphere-2025-3790
Preprint. Discussion started: 15 August 2025

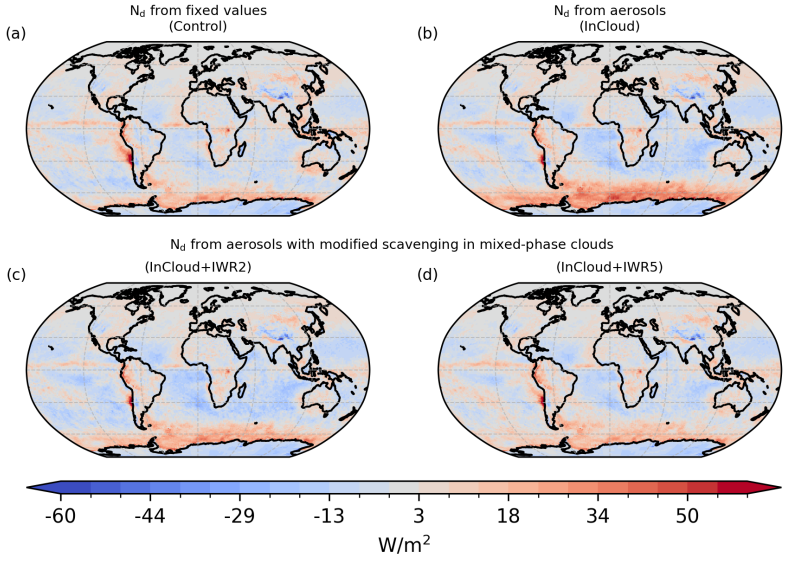

Figure 14. TOA SW flux, CERES minus IFS for the season DJF 2023-2024. IFS setups are: a) control, where N_d and r_e do not depend on aerosols; for b), c) and d) N_d and r_e are computed from aerosols at cloud level (InCloud). c) uses phase-dependent aerosol wet scavenging for mixed-phase clouds labelled as IWR2 d) includes additional changes to improve aerosol scavenging in mixed-phase conditions and is labelled as IWR5.

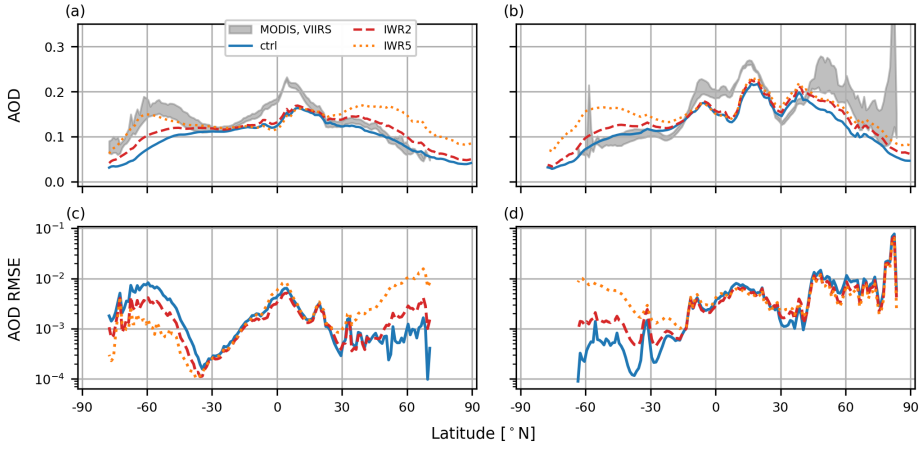

Figure 15. Zonal mean (left) and zonal RMSE (right) for seasonal 550 nm AOD for the DJF 2023-2024 season (top) and the JJA 2024 season (bottom). We included only points over sea, where the MODIS pixel count for AOD was larger than 150 and VIIRS had at least 7 days of valid retrievals.

https://doi.org/10.5194/egusphere-2025-3790
Preprint. Discussion started: 15 August 2025

winter hemisphere. This suggests that the simulated seasonal cycle of aerosol emissions might need improvement. The CAMS aerosols tend to underpredict AE over high latitude seas, which is probably due to too large AOD contribution from coarse sea salt ($r \geq 1\ \mu\mathrm{m}$). Such evidence might point at issues with the aerosol speciation in these regions. Possible areas of improvement could involve the seasonal cycle of emissions for dimethyl sulfide (DMS) and the amount of biogenic marine organic aerosol contained in sea spray.

Code availability. The IFS code is the intellectual property of ECMWF and its member states, and therefore it is not publicly available. Access to the IFS code updated to version CY48R1 can be obtained from ECMWF under a free OpenIFS licence. The code used to simulate optical properties uses the Scott Prahl's Miepython library (https://github.com/scottprahl/miepython).

Appendix A: Conversion from mixed bulk-bin to bulk representation of sea salt aerosol

Sea salt aerosol is represented by a bimodal distribution whose domain is partitioned into three intervals, or bins. Each of these bins is assigned to a different tracer; so that three sea salt aerosol species are defined: fine, medium and coarse (bins 1 to 3). This means that we need to define a function mapping the mixed bulk-bin to the bulk representation used for the activation scheme. In general, it is not possible to find a conversion strategy that preserves all moments of the distribution, due to the fact that the mixed bulk-bin representation allows discontinuities at the boundaries of each interval bin. In this study, we decided to map the three bins of a bimodal distribution onto the two modes of the same distribution, thus defining two sea salt ccn species to use in the activation scheme. Let $n_i(r) = \mathrm{d}N/\mathrm{d}r(r)$ the b-th mode of the number PSD, α_i the relative weight assigned to the mode ($\sum_i \alpha_i = 1$) and Φ_b the interval defining the domain for the bin species b. The total mass of a species M_b is given by the sum of the masses projecting on the two PSD modes:

$$M_b = \sum_i M_{b,i} = \sum_i \frac{4}{3}\pi\rho \int_{\Phi_b} r^3 \alpha_i n_i(r)\, \mathrm{d}r \tag{A1}$$

where ρ is the mass density. By taking the ratio $q_{b,i} = M_{b,i}/M_b$ one knows which fraction of the mass of the bin species b must be assigned to the i-th mode of the original distribution. This results in the fractional contributions of the three sea salt bins to the two sea salt ccn species.

However, while this method ensures that the mapping across representations conserves total mass, it does not constrain particle numbers. The only (particular) case when particle numbers are preserved is when the ratio between the mass concentrations of the three sea salt species is such that the merged distribution resulting from it is smooth.

https://doi.org/10.5194/egusphere-2025-3790
Preprint. Discussion started: 15 August 2025

Appendix B: Relationship between AOD and particle numbers in a bulk representation

Optical thickness per unit mass (here indicated with t) of a unit volume homogeneously filled by a total mass M of an aerosol species given by:

$$t \equiv \tau/M = \pi \frac{N}{M} \int r^2 Q_{\text{sca}} n(r)\, \mathrm{d}r \tag{B1}$$

where $n(r)$ is the normalized number distribution. If we consider as a rough approximation (for an ideal case with small enough σ) $Q \approx q\, r^k$ (where $k = 6$ in the Rayleigh scattering regime, for purely real refractive index) and use the notable expressions for the momenta of a log-normal distribution:

$$\begin{aligned} t &\approx \frac{q}{4/3\pi\rho} \frac{E[r^{k+2}]}{E[r^3]} \\ &\approx \frac{q}{4/3\pi\rho} e^{(k-1)\mu}\, e^{(k^2+2k-5)\sigma^2} \end{aligned} \tag{B2}$$

More straightforwardly, the number of particles per unit mass (hereby with n_a) is given from the identity between total mass M and number of particles N:

$$n_a \equiv \frac{N_a}{M} = \frac{1}{4/3\pi\rho} e^{-3\mu}\, e^{-9\sigma^2} \tag{B3}$$

The amount of droplet is then a non-trivial but monotonic function of n_a.

These relationships illustrate that, in a bulk representation, increasing/decreasing the burden of an aerosol species determines a proportional variation in both τ and N_a. However, changing μ and σ impacts τ and N_a in regime-depending directions:

$$\frac{\mathrm{d}t}{\mathrm{d}\mu} \approx (k-1)\, t \tag{B4}$$

$$\frac{\mathrm{d}t}{\mathrm{d}\sigma} \approx (k^2+k-5)\sigma\, t \tag{B5}$$

$$\frac{\mathrm{d}n_a}{\mathrm{d}\mu} = -3\, n_a \tag{B6}$$

$$\frac{\mathrm{d}n_a}{\mathrm{d}\sigma} = -18\sigma\, n_a \tag{B7}$$

In the case of $r \ll \lambda$, it is asymptotically satisfied that Q_{sca} grows faster than linear, i.e. $k > 1$, with $k = 6$ for the Rayleigh non-absorbing regime. In all these cases increasing/decreasing the median radius $r_{\text{med}} = \log(\mu)$ inversely affects the optical thickness of the species. For larger radii, In the geometric optics regime, $q \approx 2$, $k \approx 0$, so that a smaller median radius implies the tracer to be optically thicker. The ratio between light wavelength and particle size, as well as the orientation of the refractive index in complex space, define the response regime for AOD to PSD definition.

Appendix C: Aerosol mass burden errors from activation rates in the IFS wet scavenging scheme.

The wet scavenging scheme is expected to underestimate removal of all species we used as CCN except BC. In fact, for each aerosol the dissolved mass fraction for warm-phase conditions is given by a prescribed value: namely 0.9 for SS, 0.8 AM

https://doi.org/10.5194/egusphere-2025-3790
Preprint. Discussion started: 15 August 2025

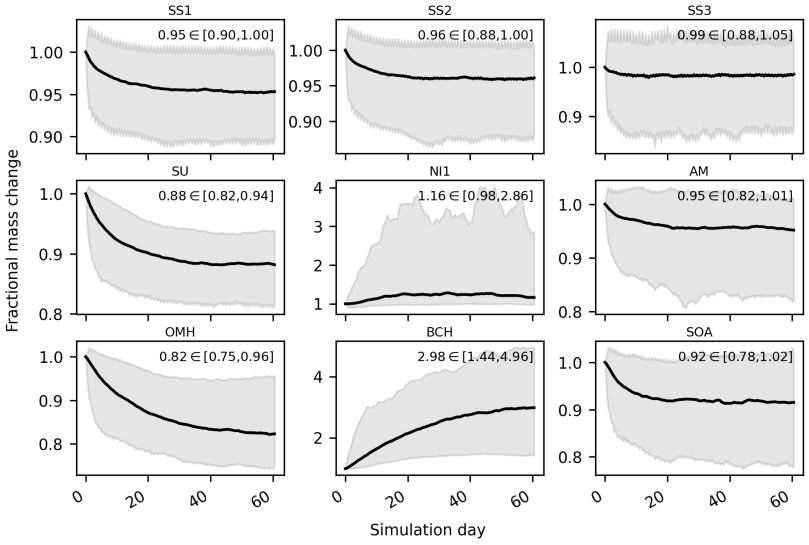

Figure C1. Change in total aerosol mass of several species from using in-cloud scavenging rates diagnosed by the aerosol activation scheme instead of the default fixed IFS values. Solid line is the median relative change (experiment divided by control), shadings are the 5th and 95th percentiles. For each panel, values for the last time-step (day 60) are reported.

and NI, 0.7 for every other hydrophilic species. Typical dissolved activated mass fraction values provided by the activation scheme are close to 1 for all species excluding black carbon, in line with approaches adopted in global chemical transport models (see e.g. Wang et al. (2014)). This is due to the mass-domination of the large fraction of most aerosol species, even those with relatively-low hygroscopicity like OM, while significant variability in activated mass fraction is associated with BC, due to low hygroscopicity and, most importantly, small typical particle size. (see figure 2). Therefore, Figure C1 shows the global relative change in total column aerosol mass given by a simulation where the mass scavenging rates were diagnosed by the wet-scavenging scheme from the aerosol activation scheme; the actual impact is limited within 10% for most species and within 80% for NI and OM. This means that the too low mass scavenging rates of the current wet scavenging scheme can explain only a small fraction of the excess particle numbers for sulfates, nitrates and organics CCN.

Author contributions. PA: conceptualization, data curation, formal analysis, investigation, methodology,software, visualization, writing (original draft preparation); MDF: conceptualization, methodology, software, writing (review and editing); RJH: conceptualization, supervision, writing (review and editing); RMF: conceptualization, supervision, writing (review and editing); SR: data curation, writing (review and editing); BB: supervision, writing (review and editing); UL: supervision, writing (review and editing)

https://doi.org/10.5194/egusphere-2025-3790
Preprint. Discussion started: 15 August 2025

Competing interests. The authors declare that they have no conflict of interest.

Acknowledgements. We thank the AERONET PIs Alexander Mangold , Alexis Merlaud, Anatoli Chaikovsky , Corinne Galy-Lacaux , David Lehmann, Elena Lind, Fabiola Tata, Grzegorz Karasinski , Ihab Abboud , Jacobo Salvador , Lynn Ma, Margarida Fernandes Ventura, Michel Van Roozendal , Norm O'Neill , Patric Seifert, Pawan Gupta , Philippe Goloub, Piotr Glowacki , Piotr Sobolewski , Pr Veronique Yoboue, Rachel T. Pinker, Raul D'Elia , Raul R. Cordero, Richard Damoah , Rick Wagener , Victoria E. Cachorro Revilla, Vitali Fioletov and their staff for establishing and maintaining the sites used for this investigation.

We thank the community of developers of the Matplotlib and Xarray projects.

We acknowledge the work of Crameri et al. (2020) for the colormaps we used for plotting data.

We thank the CAMS researchers at ECMWF, with special regards to Enza di Tomaso and Mark Parrington for the discussions about the current state of GFAS and Johannes Flemming for the frequent feedbacks on the development of this research.

Financial support.

This study was conducted within the STEP-UP! Fellowship programme funded by the Deutscher Wetterdienst (DWD) and Forschungszentrum Jülich (FZJ) and materially supported by ECMWF in collaboration with the Center for Earth System Observation and Computational analysis (CESOC).

https://doi.org/10.5194/egusphere-2025-3790
Preprint. Discussion started: 15 August 2025

References

Ahlgrimm, M., Forbes, R. M., Hogan, R. J., and Sandu, I.: Understanding Global Model Systematic Shortwave Radiation Errors in Subtropical Marine Boundary Layer Cloud Regimes, Journal of Advances in Modeling Earth Systems, 10, 2042–2060, https://doi.org/10.1029/2018MS001346, 2018.

Albrecht, B. A.: Aerosols, Cloud Microphysics, and Fractional Cloudiness, Science, 245, 1227–1230, https://doi.org/10.1126/science.245.4923.1227, 1989.

Baklanov, A., Brunner, D., Carmichael, G., Flemming, J., Freitas, S., Gauss, M., Hov, O. y., Mathur, R., Schlünzen, K. H., Seigneur, C., and Vogel, B.: Key Issues for Seamless Integrated Chemistry–Meteorology Modeling, Bulletin of the American Meteorological Society, 98, 2285–2292, https://doi.org/10.1175/BAMS-D-15-00166.1, 2017.

Bellouin, N., Rae, J., Jones, A., Johnson, C., Haywood, J., and Boucher, O.: Aerosol Forcing in the Climate Model Intercomparison Project (CMIP5) Simulations by HadGEM2-ES and the Role of Ammonium Nitrate, Journal of Geophysical Research, 116, D20 206, https://doi.org/10.1029/2011JD016074, 2011.

Bellouin, N., Quaas, J., Gryspeerdt, E., Kinne, S., Stier, P., Watson-Parris, D., Boucher, O., Carslaw, K. S., Christensen, M., Daniau, A.-L., Dufresne, J.-L., Feingold, G., Fiedler, S., Forster, P., Gettelman, A., Haywood, J. M., Lohmann, U., Malavelle, F., Mauritsen, T., McCoy, D. T., Myhre, G., Mülmenstädt, J., Neubauer, D., Possner, A., Rugenstein, M., Sato, Y., Schulz, M., Schwartz, S. E., Sourdeval, O., Storelvmo, T., Toll, V., Winker, D., and Stevens, B.: Bounding Global Aerosol Radiative Forcing of Climate Change, Reviews of Geophysics, 58, e2019RG000 660, https://doi.org/10.1029/2019RG000660, 2020.

Benedetti, A., Morcrette, J., Boucher, O., Dethof, A., Engelen, R. J., Fisher, M., Flentje, H., Huneeus, N., Jones, L., Kaiser, J. W., Kinne, S., Mangold, A., Razinger, M., Simmons, A. J., and Suttie, M.: Aerosol analysis and forecast in the European Centre for Medium-Range Weather Forecasts Integrated Forecast System: 2. Data assimilation, Journal of Geophysical Research: Atmospheres, 114, 2008JD011 115, https://doi.org/10.1029/2008JD011115, 2009.

Bodas-Salcedo, A., Williams, K. D., Ringer, M. A., Beau, I., Cole, J. N. S., Dufresne, J.-L., Koshiro, T., Stevens, B., Wang, Z., and Yokohata, T.: Origins of the Solar Radiation Biases over the Southern Ocean in CFMIP2 Models*, Journal of Climate, 27, 41–56, https://doi.org/10.1175/JCLI-D-13-00169.1, 2014.

Bozzo, A., Benedetti, A., Flemming, J., Kipling, Z., and Rémy, S.: An aerosol climatology for global models based on the tropospheric aerosol scheme in the Integrated Forecasting System of ECMWF, Geoscientific Model Development, 13, 1007–1034, https://doi.org/10.5194/gmd-13-1007-2020, 2020.

C3S: ERA5 Hourly Data on Single Levels from 1940 to Present, https://doi.org/10.24381/CDS.ADBB2D47, 2018.

Crameri, F., Shephard, G. E., and Heron, P. J.: The Misuse of Colour in Science Communication, Nature Communications, 11, 5444, https://doi.org/10.1038/s41467-020-19160-7, 2020.

Doelling, D.: CERES Energy Balanced and Filled (EBAF) TOA Monthly Means Data in netCDF Edition4.2, https://doi.org/10.5067/TERRA-AQUA-NOAA20/CERES/EBAF-TOA_L3B004.2, 2022.

Dubovik, O. and King, M. D.: A flexible inversion algorithm for retrieval of aerosol optical properties from Sun and sky radiance measurements, Journal of Geophysical Research: Atmospheres, 105, 20 673–20 696, https://doi.org/10.1029/2000JD900282, 2000.

ECMWF: IFS Documentation CY49R1 - Part VIII: Atmospheric Composition, Tech. rep., https://doi.org/10.21957/D13AF18259, publisher: ECMWF, 2024.

https://doi.org/10.5194/egusphere-2025-3790
Preprint. Discussion started: 15 August 2025

Field, P. R., Hill, A., Shipway, B., Furtado, K., Wilkinson, J., Miltenberger, A., Gordon, H., Grosvenor, D. P., Stevens, R., and Van Weverberg, K.: Implementation of a double moment cloud microphysics scheme in the UK met office regional numerical weather prediction model, Quarterly Journal of the Royal Meteorological Society, 149, 703–739, https://doi.org/10.1002/qj.4414, 2023.

Flemming, J., Huijnen, V., Arteta, J., Bechtold, P., Beljaars, A., Blechschmidt, A.-M., Diamantakis, M., Engelen, R. J., Gaudel, A., Inness, A., Jones, L., Josse, B., Katragkou, E., Marecal, V., Peuch, V.-H., Richter, A., Schultz, M. G., Stein, O., and Tsikerdekis, A.: Tropospheric Chemistry in the Integrated Forecasting System of ECMWF, Geoscientific Model Development, 8, 975–1003, https://doi.org/10.5194/gmd-8-975-2015, 2015.

Forkel, M., Wessollek, C., Huijnen, V., Andela, N., De Laat, A., Kinalczyk, D., Marrs, C., Van Wees, D., Bastos, A., Ciais, P., Fawcett, D., Kaiser, J. W., Klauberg, C., Kutchartt, E., Leite, R., Li, W., Silva, C., Sitch, S., Goncalves De Souza, J., Zaehle, S., and Plummer, S.: Burning of Woody Debris Dominates Fire Emissions in the Amazon and Cerrado, Nature Geoscience, 18, 140–147, https://doi.org/10.1038/s41561-024-01637-5, 2025.

Fossum, K. N., Ovadnevaite, J., Ceburnis, D., Preißler, J., Snider, J. R., Huang, R.-J., Zuend, A., and O'Dowd, C.: Sea-spray regulates sulfate cloud droplet activation over oceans, npj Climate and Atmospheric Science, 3, 14, https://doi.org/10.1038/s41612-020-0116-2, 2020.

Gordon, H., Glassmeier, F., and T. McCoy, D.: An Overview of Aerosol-Cloud Interactions, in: Geophysical Monograph Series, edited by Sullivan, S. C. and Hoose, C., pp. 13–45, Wiley, 1 edn., ISBN 978-1-119-70031-9 978-1-119-70035-7, https://doi.org/10.1002/9781119700357.ch2, 2023.

Grosvenor, D. P. and Wood, R.: The effect of solar zenith angle on MODIS cloud optical and microphysical retrievals within marine liquid water clouds, Atmospheric Chemistry and Physics, 14, 7291–7321, https://doi.org/10.5194/acp-14-7291-2014, 2014.

Grosvenor, D. P., Sourdeval, O., and Wood, R.: Parameterizing cloud top effective radii from satellite retrieved values, accounting for vertical photon transport: quantification and correction of the resulting bias in droplet concentration and liquid water path retrievals, Atmospheric Measurement Techniques, 11, 4273–4289, https://doi.org/10.5194/amt-11-4273-2018, 2018.

Gryspeerdt, E., McCoy, D., Crosbie, E., Moore, R. H., Nott, G. J., Painemal, D., Small-Griswold, J., Sorooshian, A., and Ziemba, L.: Cloud Droplet Number Concentration, Calculated from the MODIS (Moderate Resolution Imaging Spectroradiometer) Cloud Optical Properties Retrieval and Gridded Using Different Sampling Strategies, https://doi.org/10.5285/864A46CC65054008857EE5BB772A2A2B, 2022a.

Gryspeerdt, E., McCoy, D. T., Crosbie, E., Moore, R. H., Nott, G. J., Painemal, D., Small-Griswold, J., Sorooshian, A., and Ziemba, L.: The impact of sampling strategy on the cloud droplet number concentration estimated from satellite data, Atmospheric Measurement Techniques, 15, 3875–3892, https://doi.org/10.5194/amt-15-3875-2022, 2022b.

Gupta, P., Remer, L. A., Levy, R. C., and Mattoo, S.: Validation of MODIS 3 km land aerosol optical depth from NASA's EOS Terra and Aqua missions, Atmospheric Measurement Techniques, 11, 3145–3159, https://doi.org/10.5194/amt-11-3145-2018, 2018.

Hogan, R. J., Grant, A. L. M., Illingworth, A. J., Pearson, G. N., and O'Connor, E. J.: Vertical Velocity Variance and Skewness in Clear and Cloud-topped Boundary Layers as Revealed by Doppler Lidar, Quarterly Journal of the Royal Meteorological Society, 135, 635–643, https://doi.org/10.1002/qj.413, 2009.

Holben, B., Eck, T., Slutsker, I., Tanré, D., Buis, J., Setzer, A., Vermote, E., Reagan, J., Kaufman, Y., Nakajima, T., Lavenu, F., Jankowiak, I., and Smirnov, A.: AERONET—A Federated Instrument Network and Data Archive for Aerosol Characterization, Remote Sensing of Environment, 66, 1–16, https://doi.org/10.1016/S0034-4257(98)00031-5, 1998.

Hoose, C., Lohmann, U., Stier, P., Verheggen, B., and Weingartner, E.: Aerosol processing in mixed-phase clouds in ECHAM5-HAM: Model description and comparison to observations, Journal of Geophysical Research: Atmospheres, 113, 2007JD009 251, https://doi.org/10.1029/2007JD009251, 2008.

https://doi.org/10.5194/egusphere-2025-3790
Preprint. Discussion started: 15 August 2025

Hoppel, W. A., Fitzgerald, J. W., Frick, G. M., Larson, R. E., and Mack, E. J.: Aerosol Size Distributions and Optical Properties Found in the Marine Boundary Layer over the Atlantic Ocean, Journal of Geophysical Research: Atmospheres, 95, 3659–3686, https://doi.org/10.1029/JD095iD04p03659, 1990.

Hsu, N. C., Jeong, M.-J., Bettenhausen, C., Sayer, A. M., Hansell, R., Seftor, C. S., Huang, J., and Tsay, S.-C.: Enhanced Deep Blue Aerosol Retrieval Algorithm: The Second Generation, Journal of Geophysical Research: Atmospheres, 118, 9296–9315, https://doi.org/10.1002/jgrd.50712, 2013.

Jones, A., Roberts, D. L., Woodage, M. J., and Johnson, C. E.: Indirect Sulphate Aerosol Forcing in a Climate Model with an Interactive Sulphur Cycle, Journal of Geophysical Research: Atmospheres, 106, 20 293–20 310, https://doi.org/10.1029/2000JD000089, 2001.

Kaiser, J. W., Heil, A., Andreae, M. O., Benedetti, A., Chubarova, N., Jones, L., Morcrette, J.-J., Razinger, M., Schultz, M. G., Suttie, M., and Van Der Werf, G. R.: Biomass Burning Emissions Estimated with a Global Fire Assimilation System Based on Observed Fire Radiative Power, Biogeosciences, 9, 527–554, https://doi.org/10.5194/bg-9-527-2012, 2012.

Levy, R. C., Mattoo, S., Munchak, L. A., Remer, L. A., Sayer, A. M., Patadia, F., and Hsu, N. C.: The Collection 6 MODIS Aerosol Products over Land and Ocean, Atmospheric Measurement Techniques, 6, 2989–3034, https://doi.org/10.5194/amt-6-2989-2013, 2013.

Liu, M. and Matsui, H.: Improved Simulations of Global Black Carbon Distributions by Modifying Wet Scavenging Processes in Convective and Mixed-Phase Clouds, Journal of Geophysical Research: Atmospheres, 126, e2020JD033 890, https://doi.org/10.1029/2020JD033890, 2021.

Liu, Y., Daum, P. H., McGraw, R., and Wood, R.: Parameterization of the Autoconversion Process. Part II: Generalization of Sundqvist-Type Parameterizations, Journal of the Atmospheric Sciences, 63, 1103–1109, https://doi.org/10.1175/JAS3675.1, 2006.

Luo, G., Yu, F., and Schwab, J.: Revised treatment of wet scavenging processes dramatically improves GEOS-Chem 12.0.0 simulations of surface nitric acid, nitrate, and ammonium over the United States, Geoscientific Model Development, 12, 3439–3447, https://doi.org/10.5194/gmd-12-3439-2019, 2019.

Maddux, B. C., Ackerman, S. A., and Platnick, S.: Viewing Geometry Dependencies in MODIS Cloud Products, Journal of Atmospheric and Oceanic Technology, 27, 1519–1528, https://doi.org/10.1175/2010JTECHA1432.1, 2010.

McCoy, D. T., Burrows, S. M., Wood, R., Grosvenor, D. P., Elliott, S. M., Ma, P.-L., Rasch, P. J., and Hartmann, D. L.: Natural aerosols explain seasonal and spatial patterns of Southern Ocean cloud albedo, Science Advances, 1, e1500 157, https://doi.org/10.1126/sciadv.1500157, 2015.

McCoy, D. T., Bender, F. A.-M., Grosvenor, D. P., Mohrmann, J. K., Hartmann, D. L., Wood, R., and Field, P. R.: Predicting Decadal Trends in Cloud Droplet Number Concentration Using Reanalysis and Satellite Data, Atmospheric Chemistry and Physics, 18, 2035–2047, https://doi.org/10.5194/acp-18-2035-2018, 2018.

McFarquhar, G. M., Bretherton, C. S., Marchand, R., Protat, A., DeMott, P. J., Alexander, S. P., Roberts, G. C., Twohy, C. H., Toohey, D., Siems, S., Huang, Y., Wood, R., Rauber, R. M., Lasher-Trapp, S., Jensen, J., Stith, J. L., Mace, J., Um, J., Järvinen, E., Schnaiter, M., Gettelman, A., Sanchez, K. J., McCluskey, C. S., Russell, L. M., McCoy, I. L., Atlas, R. L., Bardeen, C. G., Moore, K. A., Hill, T. C. J., Humphries, R. S., Keywood, M. D., Ristovski, Z., Cravigan, L., Schofield, R., Fairall, C., Mallet, M. D., Kreidenweis, S. M., Rainwater, B., D'Alessandro, J., Wang, Y., Wu, W., Saliba, G., Levin, E. J. T., Ding, S., Lang, F., Truong, S. C. H., Wolff, C., Haggerty, J., Harvey, M. J., Klekociuk, A. R., and McDonald, A.: Observations of Clouds, Aerosols, Precipitation, and Surface Radiation over the Southern Ocean: An Overview of CAPRICORN, MARCUS, MICRE, and SOCRATES, Bulletin of the American Meteorological Society, 102, E894–E928, https://doi.org/10.1175/BAMS-D-20-0132.1, 2021.

https://doi.org/10.5194/egusphere-2025-3790
Preprint. Discussion started: 15 August 2025

Menon, S., Genio, A. D. D., Koch, D., and Tselioudis, G.: GCM Simulations of the Aerosol Indirect Effect: Sensitivity to Cloud Parameterization and Aerosol Burden, Journal of the Atmospheric Sciences, 59, 692–713, https://doi.org/10.1175/1520-0469(2002)059<0692:GSOTAI>2.0.CO;2, 2002.

Mulcahy, J. P., Walters, D. N., Bellouin, N., and Milton, S. F.: Impacts of Increasing the Aerosol Complexity in the Met Office Global Numerical Weather Prediction Model, Atmospheric Chemistry and Physics, 14, 4749–4778, https://doi.org/10.5194/acp-14-4749-2014, 2014.

Mulcahy, J. P., Jones, C., Sellar, A., Johnson, B., Boutle, I. A., Jones, A., Andrews, T., Rumbold, S. T., Mollard, J., Bellouin, N., Johnson, C. E., Williams, K. D., Grosvenor, D. P., and McCoy, D. T.: Improved Aerosol Processes and Effective Radiative Forcing in HadGEM3 and UKESM1, Journal of Advances in Modeling Earth Systems, 10, 2786–2805, https://doi.org/10.1029/2018MS001464, 2018.

Nakajima, T. and King, M. D.: Determination of the Optical Thickness and Effective Particle Radius of Clouds from Reflected Solar Radiation Measurements. Part I: Theory, Journal of the Atmospheric Sciences, 47, 1878–1893, https://doi.org/10.1175/1520-0469(1990)047<1878:DOTOTA>2.0.CO;2, 1990.

Palmer, T. N., Doblas-Reyes, F. J., Weisheimer, A., and Rodwell, M. J.: Toward Seamless Prediction: Calibration of Climate Change Projections Using Seasonal Forecasts, Bulletin of the American Meteorological Society, 89, 459–470, https://doi.org/10.1175/BAMS-89-4-459, 2008.

Penner, J. E., Quaas, J., Storelvmo, T., Takemura, T., Boucher, O., Guo, H., Kirkeva, A., and Seland, O.: Model Intercomparison of Indirect Aerosol Effects, Atmos. Chem. Phys., 2006.

Petters, M. D. and Kreidenweis, S. M.: A single parameter representation of hygroscopic growth and cloud condensation nucleus activity, Atmospheric Chemistry and Physics, 2007.

Petty, G. W.: A First Course in Atmospheric Radiation, Sundog Publ, 2. ed edn., ISBN 978-0-9729033-1-8, 2006.

Pincus, R. and Baker, M. B.: Effect of Precipitation on the Albedo Susceptibility of Clouds in the Marine Boundary Layer, Nature, 372, 250–252, https://doi.org/10.1038/372250a0, 1994.

Platnick, S., King, M., and Hubanks, P.: MODIS (Aqua) Atmosphere L3 Monthly Product, NASA MODIS Adaptive Processing System, Goddard Space Flight Center, https://doi.org/10.5067/MODIS/MYD08_M3.061, 2017a.

Platnick, S., King, M., and Hubanks, P.: MODIS (Terra) Atmosphere L3 Monthly Product, NASA MODIS Adaptive Processing System, Goddard Space Flight Center, https://doi.org/10.5067/MODIS/MOD08_M3.061, 2017b.

Platnick, S., Meyer, K. G., King, M. D., Wind, G., Amarasinghe, N., Marchant, B., Arnold, G. T., Zhang, Z., Hubanks, P. A., Holz, R. E., Yang, P., Ridgway, W. L., and Riedi, J.: The MODIS Cloud Optical and Microphysical Products: Collection 6 Updates and Examples From Terra and Aqua, IEEE Transactions on Geoscience and Remote Sensing, 55, 502–525, https://doi.org/10.1109/TGRS.2016.2610522, 2017c.

Pruppacher, H. and Klett, J.: Microphysics of Clouds and Precipitation, vol. 18 of *Atmospheric and Oceanographic Sciences Library*, Springer Netherlands, Dordrecht, ISBN 978-0-7923-4211-3 978-0-306-48100-0, https://doi.org/10.1007/978-0-306-48100-0, 2010.

Qi, L., Li, Q., He, C., Wang, X., and Huang, J.: Effects of the Wegener–Bergeron–Findeisen process on global black carbon distribution, Atmospheric Chemistry and Physics, 17, 7459–7479, https://doi.org/10.5194/acp-17-7459-2017, 2017.

Quaas, J. and Gryspeerdt, E.: Aerosol-cloud interactions in liquid clouds, in: Aerosols and Climate, pp. 489–544, Elsevier, ISBN 978-0-12-819766-0, https://doi.org/10.1016/B978-0-12-819766-0.00019-5, 2022.

Rasch, P. J. and Carslaw, K. S.: Aerosol–Climate Modeling, in: Aerosols and Climate, pp. 187–248, Elsevier, ISBN 978-0-12-819766-0, https://doi.org/10.1016/B978-0-12-819766-0.00009-2, 2022.

https://doi.org/10.5194/egusphere-2025-3790
Preprint. Discussion started: 15 August 2025

Reutter, P., Su, H., Trentmann, J., Simmel, M., Rose, D., Gunthe, S. S., Wernli, H., Andreae, M. O., and Poschl, U.: Aerosol- and Updraft-Limited Regimes of Cloud Droplet Formation: Influence of Particle Number, Size and Hygroscopicity on the Activation of Cloud Condensation Nuclei (CCN), Atmos. Chem. Phys., 2009.

Rothenberg, D. and Wang, C.: Metamodeling of Droplet Activation for Global Climate Models, Journal of the Atmospheric Sciences, 73, 1255–1272, https://doi.org/10.1175/JAS-D-15-0223.1, 2016.

Rémy, S., Kipling, Z., Huijnen, V., Flemming, J., Nabat, P., Michou, M., Ades, M., Engelen, R., and Peuch, V.-H.: Description and evaluation of the tropospheric aerosol scheme in the Integrated Forecasting System (IFS-AER, cycle 47R1) of ECMWF, Geoscientific Model Development, 15, 4881–4912, https://doi.org/10.5194/gmd-15-4881-2022, 2022.

Sayer, A. M., Munchak, L. A., Hsu, N. C., Levy, R. C., Bettenhausen, C., and Jeong, M.-J.: MODIS Collection 6 Aerosol Products: Comparison between Aqua's e-Deep Blue, Dark Target, and "Merged" Data Sets, and Usage Recommendations, Journal of Geophysical Research: Atmospheres, 119, https://doi.org/10.1002/2014JD022453, 2014.

Sayer, A. M., Hsu, N. C., Lee, J., Bettenhausen, C., Kim, W. V., and Smirnov, A.: Satellite Ocean Aerosol Retrieval (SOAR) Algorithm Extension to S-NPP VIIRS as Part of the "Deep Blue" Aerosol Project, Journal of Geophysical Research: Atmospheres, 123, 380–400, https://doi.org/10.1002/2017JD027412, 2018.

Sellegri, K., Simó, R., Wang, B., Alpert, P. A., Altieri, K., Burrows, S., Hopkins, F. E., Koren, I., McCoy, I. L., Ovadnevaite, J., Salter, M., and Schmale, J.: Influence of open ocean biogeochemistry on aerosol and clouds: Recent findings and perspectives, Elem Sci Anth, 12, 00 058, https://doi.org/10.1525/elementa.2023.00058, 2024.

SSEC, V.: VIIRS/NOAA20 Deep Blue Level 3 Monthly Aerosol Data, 1 Degree X1 Degree Grid, https://doi.org/10.5067/VIIRS/AERDB_M3_VIIRS_NOAA20.002, 2023a.

SSEC, V.: VIIRS/SNPP Deep Blue Level 3 Monthly Aerosol Data, 1 Degree X1 Degree Grid, https://doi.org/10.5067/VIIRS/AERDB_M3_VIIRS_SNPP.002, 2023b.

Stier, P., Feichter, J., Kinne, S., Kloster, S., Vignati, E., Wilson, J., Ganzeveld, L., Tegen, I., Werner, M., Balkanski, Y., Schulz, M., Boucher, O., Minikin, A., and Petzold, A.: The aerosol-climate model ECHAM5-HAM, Atmos. Chem. Phys., 2005.

Szopa, S., Naik, V., Adhikary, B., Artaxo, P., Berntsen, T., W.D. Collins, S. Fuzzi, L. Gallardo, A. Kiendler-Scharr, Z. Klimont, H. Liao, N. Unger, and P. Zanis: The Earth's Energy Budget, Climate Feedbacks, and Climate Sensitivity, in: Climate Change 2021: The Physical Science Basis. Contribution of Working Group I to the Sixth Assessment Report of the Intergovernmental Panel on Climate Change, Cambridge University Press, 1 edn., ISBN 978-1-00-915789-6, https://doi.org/10.1017/9781009157896, 2023.

Tegen, I., Hollrig, P., Chin, M., Fung, I., Jacob, D., and Penner, J.: Contribution of Different Aerosol Species to the Global Aerosol Extinction Optical Thickness: Estimates from Model Results, Journal of Geophysical Research: Atmospheres, 102, 23 895–23 915, https://doi.org/10.1029/97JD01864, 1997.

Teng, S., Liu, C., Schnaiter, M., Chakrabarty, R. K., and Liu, F.: Accounting for the effects of nonideal minor structures on the optical properties of black carbon aerosols, Atmospheric Chemistry and Physics, 19, 2917–2931, https://doi.org/10.5194/acp-19-2917-2019, 2019.

Twomey, S.: The Influence of Pollution on the Shortwave Albedo of Clouds, Journal of the Atmospheric Sciences, 34, 1149–1152, https://doi.org/10.1175/1520-0469(1977)034<1149:TIOPOT>2.0.CO;2, 1977.

Twomey, S.: Aerosols, clouds and radiation, Atmospheric Environment. Part A. General Topics, 25, 2435–2442, https://doi.org/10.1016/0960-1686(91)90159-5, 1991.

https://doi.org/10.5194/egusphere-2025-3790
Preprint. Discussion started: 15 August 2025

Verheggen, B., Cozic, J., Weingartner, E., Bower, K., Mertes, S., Connolly, P., Gallagher, M., Flynn, M., Choularton, T., and Baltensperger, U.: Aerosol partitioning between the interstitial and the condensed phase in mixed-phase clouds, Journal of Geophysical Research: Atmospheres, 112, 2007JD008 714, https://doi.org/10.1029/2007JD008714, 2007.

Wang, Q., Jacob, D. J., Spackman, J. R., Perring, A. E., Schwarz, J. P., Moteki, N., Marais, E. A., Ge, C., Wang, J., and Barrett, S. R. H.: Global budget and radiative forcing of black carbon aerosol: Constraints from pole-to-pole (HIPPO) observations across the Pacific, Journal of Geophysical Research: Atmospheres, 119, 195–206, https://doi.org/10.1002/2013JD020824, 2014.

Wang, X., Gordon, H., Grosvenor, D. P., Andreae, M. O., and Carslaw, K. S.: Contribution of Regional Aerosol Nucleation to Low-Level CCN in an Amazonian Deep Convective Environment: Results from a Regionally Nested Global Model, Atmospheric Chemistry and Physics, 23, 4431–4461, https://doi.org/10.5194/acp-23-4431-2023, 2023.

West, R. E. L., Stier, P., Jones, A., Johnson, C. E., Mann, G. W., Bellouin, N., Partridge, D. G., and Kipling, Z.: The importance of vertical velocity variability for estimates of the indirect aerosol effects, Atmospheric Chemistry and Physics, 14, 6369–6393, https://doi.org/10.5194/acp-14-6369-2014, 2014.

Wielicki, B. A., Barkstrom, B. R., Harrison, E. F., Lee, R. B., Louis Smith, G., and Cooper, J. E.: Clouds and the Earth's Radiant Energy System (CERES): An Earth Observing System Experiment, Bulletin of the American Meteorological Society, 77, 853–868, https://doi.org/10.1175/1520-0477(1996)077<0853:CATERE>2.0.CO;2, 1996.

Yu, H., Li, W., Zhang, Y., Tunved, P., Dall'Osto, M., Shen, X., Sun, J., Zhang, X., Zhang, J., and Shi, Z.: Organic coating on sulfate and soot particles during late summer in the Svalbard Archipelago, Atmospheric Chemistry and Physics, 19, 10 433–10 446, https://doi.org/10.5194/acp-19-10433-2019, 2019.